A Capillary Bundle Model for the Electrical Conductivity of Saturated Frozen Porous Media

Haoliang Luo, Damien Jougnot, Anne Jost, Jidong Teng, Luong Duy Thanh

JGR Solid Earth

Key Points:

- A novel physically-based model for electrical conductivity of the saturated frozen soils is developed, using the Gibbs-Thomson effect and surface complexation model
- The influences of bulk and surface conductivities are considered and surface conductivity is linked with pore size distribution and cation exchange capacity
- The proposed model successfully predicts the data from the experiment described in this work and published experimental data

Correspondence to:
D. Jougnot,
damien.jougnot@upmc.fr

Author Contributions:

Conceptualization: Haoliang Luo, Damien Jougnot, Luong Duy Thanh
Data curation: Haoliang Luo, Jidong Teng
Formal analysis: Haoliang Luo, Anne Jost
Investigation: Haoliang Luo
Methodology: Damien Jougnot, Anne Jost, Luong Duy Thanh
Project Administration: Damien Jougnot, Anne Jost
Resources: Haoliang Luo, Jidong Teng
Software: Haoliang Luo, Damien Jougnot
Supervision: Damien Jougnot, Anne Jost
Writing – original draft: Haoliang Luo
Writing – review & editing: Damien Jougnot, Anne Jost, Jidong Teng, Luong Duy Thanh

A Capillary Bundle Model for the Electrical Conductivity of Saturated Frozen Porous Media

Haoliang Luo[1] , **Damien Jougnot[1]** , **Anne Jost[1]** , **Jidong Teng[2]** , and **Luong Duy Thanh[3]**

[1]CNRS, EPHE, UMR 7619 Metis, Sorbonne Université, Paris, France, [2]School of Civil Engineering, Central South University, Changsha, China, [3]Thuyloi University, Ha Noi, Vietnam

Abstract Liquid water in frozen porous media provides the path for moisture and solute migration, which is one of the essential problems to study thaw-weakening and frost-heave in freezing region engineering. Determining and monitoring liquid water saturation and permeability in saturated frozen porous media are therefore critical issues in cold regions. To this end, geophysical methods are tools of choice given their non-invasive nature. Electrical conductivity as a physical property is related to both the bulk characteristics of saturated porous medium submitted to frozen temperatures, like porosity as well as liquid water content, and surface properties, such as the solid surface-liquid water and bulk ice-liquid water interfaces. In this study, we upscale a microstructural procedure of liquid water-saturated frozen soils to predict the electrical conductivity with different pore size distributions (PSDs). Then, we analyze the model sensitivity to the model parameters and compare the lognormal and fractal PSD models. Furthermore, the proposed model successfully predicts the experimental data of electrical conductivity for different samples from experiments that are part of this work and published data. The proposed model for characterizing electrical conductivity opens up new possibilities to describe the distribution and dynamics of liquid water with geoelectrical and electromagnetic techniques in frozen environments.

Plain Language Summary Electrical and electromagnetic methods are non-invasive geophysical techniques, which have been applied to address complex environmental issues such as those encountered in cold regions, for example, the distribution and dynamics of liquid water/solute in frozen porous media, the monitoring the spatio-temporal evolution of the active layer thickness, or snowmelt infiltration. However, the application of these electrical and electromagnetic methods in cold regions requires more experimental and modeling studies of the electrical conductivity of frozen soils. In this study, we establish a physically-based capillary bundle model for describing the electrical conductivity of saturated frozen porous media with different pore size distributions. We test the accuracy of the proposed model against the experimental data described in this work and published experimental data. This physically-based approach may provide a better theoretical means to quantitate and monitor the geo-environmental problems in cold regions.

1. Introduction

Climate change tend to cause substantial changes in cold regions leading to the degradation of permafrost, instability of frozen soils and snowmelt infiltration (Li et al., 2014; Watanabe & Osada, 2016). Permafrost, an increasingly unstable component of the global climate system, controls many geophysical processes, such as the biogeochemical, hydrological cycling, as well as the permafrost-carbon cycle (Debolskiy et al., 2020; Schuur et al., 2015; Walvoord & Kurylyk, 2016). For example, the permafrost degradation increases the thickness of the active layer (the frozen zones above the permafrost that thaws and refreezes annually) and affects infrastructure stability (X. Y. Jin et al., 2022; Walvoord & Kurylyk, 2016). Particularly in seasonally frozen soil regions, the change of temperature causes structural damage and has a significant impact on the stability of the slopes (T. Wang et al., 2020; Yang et al., 2021). Therefore, there is a need for studying the degradation of permafrost and the geophysical processes of seasonally frozen soil using non-invasive geophysical tools such as those proposed in hydro-geophysics to test liquid water distribution or flow quantitatively in cold regions.

Liquid water does not experience a complete phase change into solid ice in saturated frozen porous media at a given temperature. A certain amount of liquid water, which is referred to as unfrozen liquid water, remains due to capillary action and particle surface adsorption (Kozlowski, 2007; Xu et al., 2001; J. Zhou et al., 2018). The liquid water most likely exists as a thin water film at the interface between the bulk ice and solid phases

(D. M. Anderson, 1967; D. M. Anderson & Hoekstra, 1965). The soil freezing characteristic curve (SFCC) of the porous media shows its water retention behavior during freezing or melting (Azmatch et al., 2012; Koopmans & Miller, 1966). The liquid water saturation of frozen soils is linked not only with the pore size distribution (PSD), but also with the extern factor (temperature and compaction), bulk characteristics such as electrolyte concentration and type and surface characteristics (solid surface-liquid water and bulk ice-liquid water interfaces) (Daigle, 2021; X. Jin et al., 2020; Xu et al., 2001). The liquid water provides the path for moisture and solute migration, which is the direct reason for frost heave or thaw settlement, and it is critical to evaluate the hydraulic conductivity (Teng, Liu et al., 2020; Watanabe & Flury, 2008). Therefore, accurate determination of liquid water saturation in both experimental and theoretical studies has important implications for geo-environmental problems in cold regions (Li et al., 2014; Watanabe & Osada, 2016).

In recent years, different measurement methods have been developed to measure the liquid water saturation in frozen zones, including frequency domain reflectometry (FDR), nuclear magnetic resonance (NMR), time domain reflectometry (TDR), electrical and electromagnetic methods, etc., which have good accuracy for application in cold region environment. However, the above-mentioned methods have some notable limitations. For instance, the laboratory-based NMR method calculates the liquid water content determined by the inversion results of hydrogen signal values in different states (different temperatures) by recording the energy values of hydrogen atoms in samples (e.g., Shen et al., 2020; Teng, Kou et al., 2020). Unfortunately, when used in the laboratory, this method has some limitations, notably because of the very small soil sample size or the high cost of the device, but also because it cannot measure dynamic liquid water saturation (Tan et al., 2015; X. H. Zhou et al., 2014). TDR has been widely applied in the determination of the liquid water content in frozen soils (e.g., He & Dyck, 2013; Watanabe & Wake, 2009). However, according to Yoshikawa & Overduin (2005) and X. H. Zhou et al. (2014), the liquid water content in frozen soils determined with the TDR via the relationship between the liquid water content and soil volume permittivity is often overestimated. Although only a relatively small amount of liquid water remains in the pores, it can be of paramount importance for hydrological and biogeochemical processes in cold regions, therefore justifying the need for its accurate estimation (Schuur et al., 2015; C. Wang et al., 2017).

Electrical and electromagnetic methods including the electro-magnetic induction (EMI), induced polarization (IP), electrical resistivity tomography (ERT) and self-potential (SP) methods (e.g., Chalikakis et al., 2011; Glover, 2015; Revil et al., 2012) are increasingly used to cover a larger range of applications: from the experimental measurements (Coperey, Revil, Abdulsamad, et al., 2019; Coperey, Revil, & Stutz, 2019; Kulessa et al., 2012; Mendieta et al., 2021) to tests in the field, for example, for the multi-scale, multi-dimensional and permanent monitoring of the critical zone (Duvillard et al., 2018; Mary et al., 2020; Watlet et al., 2018). These methods allow to characterize the spatial distribution of the electrical parameters (electrical conductivity, SP and so on) in a fast and non-invasive manner. Recently, these electrical and electromagnetic methods have gained a strong interest in the field of permafrost, frozen porous media as well as snowmelt infiltration, for example, to characterize the thaw layer thickness dynamics (e.g., Dafflon et al., 2013; Duvillard et al., 2018; Murton et al., 2016; Pedrazas et al., 2020) or to measure the liquid water content in frozen porous media (Coperey, Revil, Abdulsamad, et al., 2019; Ming et al., 2020; Oldenborger & LeBlanc, 2018). For instance, the zeta potential is very sensitive to the temporal evolution of snow porosity, pH and meltwater flux, which is important in snowmelt and liquid water-ice phase change systems. Therefore, Kulessa et al. (2003, 2012) developed a novel experimental snow column method to measure the zeta potential of unsaturated flow in melting snow from SP methods. Clayton (2017, 2021) present a field feasibility study to measure the percolation flux of unsaturated meltwater using the SP method within the vertical profile of a snowpack. The electrical conductivity is highly related to the basic physical properties of frozen porous medium such as porosity, liquid water content, or hydraulic conductivity. Duvillard et al. (2018, 2021) and Coperey, Revil, Abdulsamad et al. (2019), Coperey, Revil, and Stutz (2019) characterized the spatial distribution of frozen and unfrozen zones from the electrical conductivity contrasts between ice and pore water, and determined the relationship between electrical conductivity and temperature in the frozen state using laboratory IP experiments. Results revealed that the above-mentioned geophysical methods can be applied to the quantitative and qualitative study of soil hydrology at freezing temperatures. However, few literature studies have carried out quantitative experimental studies on the content of liquid water and ice in frozen porous media according to the electrical and electromagnetic methods. In a word, the geo-environmental applications of electrical and electromagnetic methods in cold regions require more experimental and modeling studies of the electrical conductivity of frozen porous media.

Based on experimental data of electrical conductivity versus temperature, some predictive electrical conductivity models have been performed, which can be categorized into three types in the literature. The first type involves empirical electrical conductivity equations established by normalizing a reference conductivity at the reference temperature (e.g., Dafflon et al., 2016; Fortier et al., 2008; Herring et al., 2019; Oldenborger & LeBlanc, 2018). However, this type of model requires known values of the frozen and the reference conductivities (at given reference temperature) and soil porosity, among other calibration information. The second type of method is the electrical conductivity model of frozen porous medium based on the electrical theory, that is using series and parallel combinations of soil, liquid water, and ice conductances (e.g., Shan et al., 2015; L. Y. Tang et al., 2018). However, empirical parameters (or fitting parameters) appear in the electrical conductivity equations of frozen soils in this case, and have no clear physical meaning. Although quite different, these two kinds of methods have two factors in common: ignoring the effect of surface conductance (occurring at the solid surface-liquid water and bulk ice-liquid water interfaces), and ignoring the effect of PSD in the expression of the electrical conductivity as a function of temperature.

In response to this shortcoming, the third type includes the capillary bundle models of electrical conductivity of frozen porous media, which consider either a variable PSD or the physical properties of the solid surface-liquid water interface. Recently, Ming et al. (2020) calculated the liquid water content in frozen soils by establishing the cylindrical capillary electrical conductivity model from a mathematical point of view. Even if the impact of PSD on electrical conductivity is considered, this model does not consider the influence of surface conductivity at the solid surface-liquid water and bulk ice-liquid water interfaces in frozen porous media, and the physical relationship between electrical conductivity and basic soil properties such as porosity, liquid water content, permeability or cation exchange capacity remains unclear. Duvillard et al. (2018) and Coperey, Revil, Abdulsamad et al. (2019) analyzed the relationship between the electrical conductivity and unfrozen water content in frozen soils using the IP method and the dynamic Stern layer model. They established the physically-based model of frozen porous media that introduces unfrozen water content (specific exponential relationship) considering the variation of the ionic concentration during the phase transition. Actually, they considered the effect of the different PSDs on the unfrozen water content and then explored their effect on the electrical conductivity. This model also considers the influence of the surface conduction at the solid surface-liquid water interface and has been applied to interpret in situ measurements. It is currently a relatively advanced method for monitoring frozen soils and determining liquid water content (Duvillard et al., 2018). However, this model ignores the influence of surface conduction at the bulk ice-liquid water interface. To the best of our knowledge, there exist no capillary bundle model under frozen conditions considering the effect of the pore water conductivity, of the different PSDs, and of the surface conductivity at the solid surface-liquid water and bulk ice-liquid water interfaces.

In this study, we deduce such a new physically-based capillary bundle model of electrical conductivity in saturated frozen porous media. The present manuscript is divided into three steps. First, we establish a capillary bundle model (pore scale) based on the impacts of the Gibbs-Thomson effect, the pore water conductivity and the specific surface conductance from the solid surface-liquid water and bulk ice-liquid water interfaces. Then we deduce the expression of electrical conductivity as a function of temperature (macroscale) using an upscaling procedure and considering the effect of different PSDs. Besides, we conduct experiments about the electrical conductivity and liquid water saturation of three different types of soils based on laboratory electrical and electromagnetic methods and NMR. Furthermore, we also test the model parameters sensitivity and compare its performance for different PSDs. Additionally, we confront the model results with various datasets: data from our new experiments, and published data. Finally, from the proposed model, we obtain an equation for the effective formation factor that is explicitly related to liquid water saturation.

2. Theoretical Developments of a New Electrical Conductivity Model in Saturated Frozen Porous Media

In the following model we consider the porous medium consisted of a bundle of capillary tubes that represents the connected pore space (e.g., Guarracino et al., 2014; Or & Tuller, 1999; Rembert et al., 2020; Thanh et al., 2019; Tuller & Or, 2001; Yu & Cheng, 2002). We consider that the pores are initially filled with liquid water (i.e., liquid water saturated). This porous medium is then subjected to temperature changes and the following developments aim at describing the evolution of the electrical conductivity of the porous medium as a function of temperature.

The bulk ice is assumed to grow cylindrically from the center of the pores, with the sample temperature is lowered below its freezing temperature (T_m), and a thin water film, which is immobile, volumetrically small and smaller
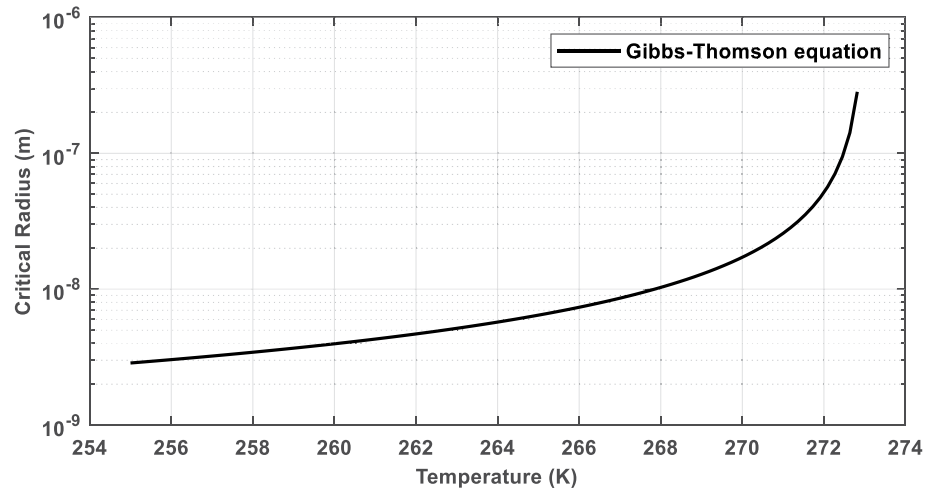
Figure 1. Evolution of the critical freezing radius with temperature as predicted by the Gibbs-Thomson equation (Equation 1).

than the thickness of the electrical double-layer of the solid surface-liquid water interface, stretches around the ice column. Capillary forces (mainly the effect of the van der Waals forces) control the phase transform of liquid water within the capillaries at equilibrium (Lebeau & Konrad, 2010, 2012; Watanabe & Flury, 2008). The Gibbs-Thomson effect shows that the largest liquid water-filled capillaries freeze first, before smaller capillaries, which shows how the depression in the freezing temperature is inversely proportional to pore radius (Ishizaki et al., 1996; Watanabe & Mizoguchi, 2002), thus there is a critical freezing radius (r_i) in the capillary tubes below freezing temperature. The pore is filled with ice when its radius is larger than the critical radius, therefore, the critical freezing radius (r_i) at corresponding temperature (T) can be obtained based on the Gibbs-Thomson equation (see Figure 1):

$$r_i = \frac{\gamma \sigma_{sl}}{L_f \rho_i} \frac{T_0}{T_0 - T}, \tag{1}$$

where σ_{sl} is the ice-liquid water interfacial free energy, $\sigma_{sl} = 0.029$ J/m^2, L_f is the latent heat of phase transformation, $L_f = 3.35 \times 10^5$ J/kg; ρ_i is the density of ice, $\rho_i = 917$ kg/m^3, T_0 is the freezing temperature of bulk liquid water (273.15 K), γ represents the shape factor of the solid-liquid interface, which is sensitive to the pore geometry. When liquid water changes into solid ice in cylindrical pores, the shape factor of solid-liquid interface is considered as 2 for freezing processes (R. Anderson et al., 2009).

Figure 2 shows the conceptual model used to predict electrical conductivity at the representative elementary volume (REV) scale (macroscale). We consider a distribution of radii of an equivalent bundle capillaries varying from a minimum to a maximum pore radius: r_{min} and r_{max}, respectively. The proposed electrical model is obtained from an upscaling procedure considering different PSDs (lognormal and fractal distributions). The electrical conductivity of a single capillary tube (i.e., microscale) is determined by the Gibbs-Thomson equation and the specific surface conductance between the solid surface-liquid water and bulk ice-liquid water interfaces, then the electrical conductivity at the REV scale is obtained by integrating the electrical conductivity of a single capillary across the entire capillary bundle.

Considering a bundle of capillary tubes, the electrical conductivity is determined by the sum of the surface and bulk electrical conduction of all capillaries. As a result, we made some of the following assumption in this study in accordance with the Gibbs-Thomson effect: (a) for $r_{min} < r < r_i$, capillaries are filled with liquid water and both the surface electrical conductivity of solid surface-liquid water interface (specific surface conductance Σ_{sw}) and the bulk conductivity are involved (Lebeau & Konrad, 2010; Or & Tuller, 1999; Thanh et al., 2020; Tuller & Or, 2001); (b) for $r_i < r < r_{max}$, capillaries are occupied by ice and water film, thus the electrical conductivity is the sum of the surface electrical conductivities at the solid surface-liquid water and bulk ice-liquid water interfaces (specific surface conductances Σ_{sw} and Σ_{iw}) (Lebeau & Konrad, 2012; R. Tang et al., 2019; Watanabe & Flury, 2008).
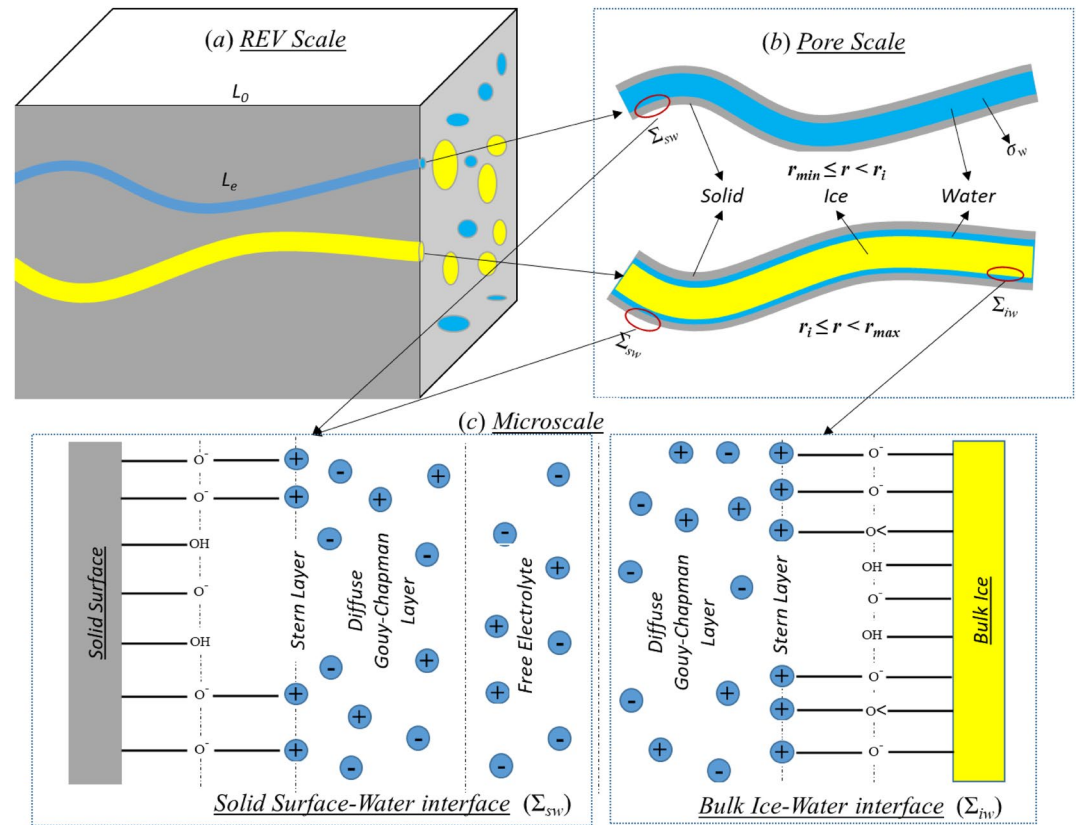
Figure 2. (a) The electrical conductivity model is including a large number of capillary tubes at the cylindrical representative elementary volume scale. (b) The tortuous capillaries follow a lognormal distribution or a fractal distribution and all the capillaries have the same tortuous length L_e (m). In accordance with the Gibbs-Thomson effect, at a given temperature, the capillary is either filled by liquid water or by ice-water film depending on its radius (pore scale). (c) Sketch representing the electrical double layer at the solid surface in contact with liquid water or at the bulk ice-liquid water interface (microscale) for a given capillary radius r.

2.1. Pore Scale

When a capillary ($r_{min} < r_1 < r_i$) of frozen soil specimen of length L_e and radius r_1 is filled by liquid water, and the resistance (R_1) of this capillary is obtained by Pfannkuch (1972), Thanh et al. (2019, 2020)

$$\frac{1}{R_1} = \frac{\pi r_1^2 \sigma_w}{L_e} + \frac{2\pi r_1 \Sigma_{sw}}{L_e}, \tag{2}$$

where σ_w (in S/m) is the electrical conductivity of the liquid water (e.g., Revil & Glover, 1997; Woodruff & Revil, 2011) and Σ_{sw} (in S) is the specific surface conductance at the solid surface-liquid water interface. If a capillary ($r_i < r_2 < r_{max}$) consists of the bulk ice and thin liquid water film, the resistance (R_2) of this capillary is

$$\frac{1}{R_2} = \frac{2\pi r_2 \Sigma_{sw}}{L_e} + \frac{2\pi r_2 \Sigma_{iw}}{L_e}, \tag{3}$$

where Σ_{iw} (in S) is the specific surface conductance at the bulk ice-liquid water interface. Consequently, the total conductance $\Sigma(r)$ of the two capillaries (one is filled with water film-bulk ice and the other is occupied by liquid water) is given by (Thanh et al., 2019, 2020)

$$\Sigma(r) = \frac{1}{R(r)} = \frac{1}{R_1} + \frac{1}{R_2}. \tag{4}$$

From Equations 2–4, the total conductance $\Sigma(r_1, r_2)$ as a function of radius is:

$$\Sigma(r_1, r_2) = \frac{\pi r_1^2 \sigma_w}{L_e} + \frac{2\pi(r_1 + r_2)\Sigma_{sw}}{L_e} + \frac{2\pi r_2 \Sigma_{iw}}{L_e}. \tag{5}$$

The first term in Equation 5 is the contribution of the pore water electrical conductivity and the second and third terms are the contributions from the specific surface conductances of solid surface-liquid water and bulk ice-liquid water interfaces. These terms are related to the electrolyte concentration. Consequently, we develop the models of the pore water conductivity and the specific surface conductances at the solid surface-liquid water and bulk ice-liquid water interfaces based on the relationship between ionic concentration and liquid water saturation and the surface complexation model. We can calculate the magnitude of the zeta potential (a key physic-chemical parameter for determining and describing the surface electrical properties of charged porous media), surface charge density as a function of salinity on the basis of the surface chemical reactions of mineral-liquid water or ice-liquid water interfaces using the surface complexation model.

2.1.1. The Model of Pore Water Conductivity

Since phase transition of liquid water from liquid to solid leads to a change in the pore water ionic concentration, the relationship between the electrolyte concentration and liquid water saturation is expressed as (e.g., Herring et al., 2019; Oldenborger & LeBlanc, 2018)

$$\frac{C_u}{C_0} = \frac{S_0}{S_u}, \tag{6}$$

where C_u is the ionic concentration in frost state (in mol/L), C_0 is the initial ionic concentration above freezing temperature (in mol/L), S_0 is the initial liquid water saturation above freezing temperature, and S_u is the liquid water saturation below freezing temperature. We can obtain the ionic concentration below the freezing point on the basis of the liquid water saturation and initial ionic concentration. Note that such approach have been also used for other kind of phase change, such as evaporation (e.g., Jougnot et al., 2010).

Based on the following equation, we can relate the electrolyte concentration to fluid electrical conductivity in the following calculations (Revil & Glover, 1997):

$$\sigma_w = \sum_i^m N_A q_i \beta_i C_i^f, \tag{7}$$

where q_i is the charge of species i in the free electrolyte (in C), N_A is the Avogadro's number (6.02×10^{23} mol^{-1}), C_i^f is the concentration of ionic species i in the free electrolyte (in mol/L), β_i is the mobility of ionic species i in the free electrolyte (in m^{2}s^{-1} V^{-1}), and it is related to temperature (e.g., Vinegar & Waxman, 1984), as follows

$$\beta_i = \beta_i^{\text{ref}}[1 + \alpha_T(T - T_{\text{ref}})], \tag{8}$$

where β_i^{ref} is the reference mobility of ionic species i in the free electrolyte at the reference temperature T_{ref} (298 K), and its values are shown in Table 1, α_T is the temperature factor and in the range 0.019–0.022/K (e.g., Coperey, Revil, Abdulsamad, et al., 2019; Coperey, Revil, & Stutz, 2019; Revil et al., 2017). Therefore, on the basis of Equations 7 and 8, the fluid conductivity can be obtained considering the effect of the temperature,

$$\sigma_w = \sum_i^n N_A q_i \beta_i^{\text{ref}} C_i^f [1 + \alpha_T(T - T_{\text{ref}})]. \tag{9}$$

2.1.2. Electrical Double-Layer Model at the Solid Surface-Liquid Water Interface

The charge at the mineral surface, consisting of the solid surface, bulk ice or air, in the development of an electrical double layer (EDL) that includes a diffuse layer with mobile ions and a Stern layer with strongly bound ions. Ions can be adsorbed as inner and outer sphere surface complexes in the Stern layer, loosing and keeping their hydration shell, respectively. In this work we hypothesis that the inner sphere surface complexes are so tightly bound to the solid surface that they do not contribute to the surface conductivity. However, a significant part of the counter-ions in the Stern layer of minerals are adsorbed as outer sphere surface complexes and behave exactly like they were in the diffuse layer. Therefore, these ions may contribute to the surface conductivity of the

Table 1
Parameter Values of the Electrical Double-Layer Model Used in This Work

Symbols	Meaning	Value	Reference
$\beta_{Na^+}^{ref}$ (m^2 s^{-1} V^{-1})	Reference mobility of ionic species Na$^+$ in the free electrolyte	5.2×10^{-8}	Zimmermann et al. (2001)
$\beta_{Cl^-}^{ref}$ (m^2 s^{-1} V^{-1})	Reference mobility of ionic species Cl$^-$ in the free electrolyte	7.9×10^{-8}	Zimmermann et al. (2001)
$\beta_{H^+}^{ref}$ (m^2 s^{-1} V^{-1})	Reference mobility of ionic species H$^+$ in the free electrolyte	3.6×10^{-7}	Zimmermann et al. (2001)
$\beta_{OH^-}^{ref}$ (m^2 s^{-1} V^{-1})	Reference mobility of ionic species OH$^-$ in the free electrolyte	2.1×10^{-7}	Zimmermann et al. (2001)
α_T (K^{-1})	Temperature factor	0.022	Coperey, Revil, Abdulsamad et al. (2019)
Γ_l^0 (Sites nm^{-2})	Total surface site density of the mineral	5	Leroy et al. (2008)
Γ_s^0 (Sites nm^{-2})	Total surface site density of the ice	5.7	Daigle (2021)
K_{XOH}	Equilibrium constant of protonation at the mineral-liquid water interface	$10^{6.73}$	Hiemstra & Riemsdijk (1990)
K_{XOH^2}	Equilibrium constant of second protonation at the mineral-liquid water interface	$10^{-0.73}$	Hiemstra & Riemsdijk (1990)
K_{XONa}	Equilibrium constant of sodium adsorption at the mineral-liquid water interface	$10^{-0.25}$	Leroy et al. (2008)
K_d	Equilibrium constant for deprotonation at the ice-liquid water interface	$10^{-7.44}$	Daigle (2021)
K_{HO}	Equilibrium constant for H$^+$ sorption on dangling O at the ice-liquid water interface	$10^{7.60}$	Daigle (2021)
K_{Na}	Equilibrium constant for sodium sorption at the ice-liquid water interface	$10^{5.2}$	Kallay et al. (2003)
K_p	Equilibrium constant for second protonation at the ice-liquid water interface	$10^{-0.062}$	Daigle (2021)
pH	pH of REV	6–8	In this work

material. For instance, some researchers (e.g., Leroy et al., 2011, 2012, 2013, 2015; Li et al., 2016) showed that considering Stern layer contribution from outer sphere adsorbed ions to surface conductivity was necessary to quantitatively interpret zeta potential measurements with a surface complexation model. Similar findings were proposed earlier by Lyklema & Minor (1998) and Revil et al. (1998), and this assumption is well accepted in the colloid and interface community (Delgado et al., 2007). Besides, some also found that an extra contribution (not from the Stern and diffuse layers) to surface conductivity was necessary to explain the zeta potential measurements on hydrophobic materials in contact with brines such as quartz, amorphous silica and air bubble (Leroy et al., 2012, 2013; Revil et al., 1998). When ions are adsorbed as outer sphere complexes in the Stern layer, the Stern layers can be connected over multiple grains and contribute to surface conductivity in the same manner than ions in the diffuse layer. Considering the bundle of capillary model presented in this study, thus the contribution of the outer sphere complexes in the Stern layer and diffuse layer to the surface conductivity should be taken into account where there is no disconnection on the pore surface. Therefore, we consider that the surface complexation model consists of two layers: first layer is mineral surface and inner sphere surface complexes in the Stern layer, and second layer is outer sphere surface complexes in the Stern layer and diffuse layer.

We can determinate the equation between the specific surface conductance and the surface charge density considering the effect of temperature (Niu et al., 2016; Revil, 2012; Revil et al., 2018):

$$\Sigma_s \approx Q_s \beta_{Na^+}^{ref}[1 + \alpha_T(T - T_{ref})], \tag{10}$$

where Σ_s is the specific surface conductance (in S), Q_s is the surface charge density of the EDLs (outer sphere surface complexes in the Stern layer and diffuse layer) (in C m^{-2}), and $\beta_{Na^+}^{ref}$ is the effective reference mobility of cations at the reference temperature ($T_{ref} = 298$ K) ($\beta_{Na^+}^{ref} = 5.20 \times 10^{-8}$ m^2 s^{-1} V^{-1}). The following development focuses on the analysis of the relationship between the zeta potential, the surface charge density in the diffuse layer and the specific surface conductance, and the electrolyte concentration in the electrical double-layer of solid surface-water and bulk ice-water interfaces.

We consider a binary symmetric electrolyte (e.g., NaCl) in contact with the silica grains and assume that the pH = 6–8. We determine the distribution of the coions and counterions at the solid surface/liquid water interface on the basis of the EDL theory (e.g., Leroy et al., 2008; Revil & Glover, 1997). Therefore, the surface

charge density Q_s^0 of the minerals surface and inner sphere surface complexes in the Stern layer as well as the surface charge density Q_s at the EDLs (outer sphere surface complexes in the Stern layer and diffuse layer) can be expressed as, respectively

$$Q_s^0 = \frac{e_0 \Gamma_1^0}{\alpha_1} \left[K_{XOH} K_{XOH^2} \left(C_{H^+}^f \right)^2 \exp\left(-\frac{2e_0 \varphi_0}{k_b T} \right) - 1 \right], \tag{11}$$

$$Q_s = -\sqrt{8\varepsilon_f k_b T C_f} \sinh\left(\frac{e_0 \varphi_d}{2k_b T} \right), \tag{12}$$

with

$$\alpha_1 = 1 + K_{XOH} C_{H^+}^f \exp\left(-\frac{e_0 \varphi_0}{k_b T} \right) + K_{XOH} K_{XOH^2} \left(C_{H^+}^f \right)^2 \exp\left(-\frac{2e_0 \varphi_0}{k_b T} \right) + K_{XONa} C_{Na^+}^f \exp\left(-\frac{e_0 \varphi_d}{k_b T} \right), \tag{13}$$

where e_0 represents the elementary charge (taken positive, $e_0 = 1.6 \times 10^{-19}$ C), Γ_1^0 (in sites nm^{-2}) is the total surface site density of the mineral, K_{XOH}, K_{XOH^2}, K_{XONa} are the associated equilibrium constants for the different mineral surface chemical reactions (X represents the silicon at the mineral surface), their specific meanings and values are shown in Table 1. We only compare the specific surface conductance between the mineral surface-water, bulk ice-water interfaces, and the contribution of the surface and bulk conduction to the electrical conductivity. Therefore, we take the same equilibrium constant values for surface reactions of any types of material (i.e., quartz sand, silty soil and clay) in order to decrease the number of parameters in the surface complexation model. The symbols $C_{Na^+}^f$, $C_{H^+}^f$ and C_f represent the concentrations of the sodium cations in the free electrolyte, the protons and the salinity in the free electrolyte (in mol/L), $C_{H^+}^f = 10^{-pH}$ and $C_{Na^+}^f = C_f$, ε_f represents the permittivity of the pore water ($\varepsilon_f = 81\varepsilon_0$, $\varepsilon_0 \sim 8.85 \times 10^{-12}$ F m^{-1}), k_b represents the Boltzmann constant (1.381×10^{-23} J K^{-1}), T is the temperature (in K), φ_0 and φ_d are, respectively, the electrical potentials of the mineral surface and of the outer sphere surface complexes (in V). The electrical potentials are related by (Leroy et al., 2008, 2012)

$$\varphi_0 - \varphi_d = \frac{Q_s^0}{C_1}, \tag{14}$$

where C_1 is the (constant) integral capacities of the Stern layer in the interface of the mineral-water, and $C_1 = 1.07$ F m^{-2} given by Leroy et al. (2008).

The global electroneutrality equation for the solid surface/liquid water interface is

$$Q_s^0 + Q_s = 0. \tag{15}$$

We use $\Gamma_1^0 = 5$ sites nm^{-2} (Armistead et al., 1969; Aydin et al., 2004) and the values of K_{XOH}, K_{XOH^2} and K_{XONa} given by Hiemstra & Riemsdijk (1990) and Leroy et al. (2008) to calculate the values of φ_d, Q_s^0 and Σ_{sw} at different concentrations based on the Equations 10–15.

2.1.3. Electrical Double-Layer Model at the Bulk Ice-Liquid Water Interface

Kallay et al. (2003) and Daigle (2021) describe the development of the surface reactions and the distribution of charge in a manner analogous to existing modes in the electrical double-layer of the bulk ice-liquid water interface. We consider that the electrolyte around the ice is NaCl, that the transport and adsorption of chloride ions are ignored during the surface reactions, as well as pH equals 6–8. Therefore, the surface charge density Q_s^0 of the ice surface and inner sphere surface complexes in the Stern layer at the bulk ice-liquid water interface as well as the surface charge density Q_s at the EDLs (outer sphere surface complexes in the Stern layer and diffuse layer) can be expressed as (Revil & Glover, 1997), respectively

$$Q_s^0 = \frac{e_0 \Gamma_s^0}{\alpha_2} \left[K_p C_{H^+}^f \exp\left(-\frac{e_0 \varphi_0}{k_b T} \right) - \frac{K_d + \frac{1}{K_{HO}}}{C_{H^+}^f} \exp\left(\frac{e_0 \varphi_0}{k_b T} \right) \right], \tag{16}$$

$$Q_s = -\sqrt{8\varepsilon_f k_b T C_f} \sinh\left(\frac{e_0 \varphi_d}{2k_b T} \right), \tag{17}$$

with

$$\alpha_2 = 1 + \left[K_d + \frac{1}{K_{HO}} + \frac{K_{Na}}{K_{HO}} C_{Na^+}^f \exp\left(-\frac{e_0 \varphi_d}{k_b T} \right) \right] \frac{\exp\left(\frac{e_0 \varphi_0}{k_b T} \right)}{C_{H^+}^f} + K_p C_{H^+}^f \exp\left(-\frac{e_0 \varphi_0}{k_b T} \right) \tag{18}$$

where Γ_s^0 (in sites nm^{-2}) is the total surface site density of the ice-liquid water interface, K_p, K_d, K_{HO} and K_{Na} are the associated equilibrium constants for the different reactions at the surface of ice, their specific meanings and values are shown in Table 1, φ_0 and φ_d are, respectively, the electrical potential at the ice surface and the zeta potential (in V). The electrical potentials are related by Kallay et al. (2003) and Daigle (2021)

$$\varphi_0 - \varphi_d = \frac{Q_s^0}{C_2}, \tag{19}$$

where C_2 is the (constant) integral capacities of the Stern layer at the bulk ice-water interface, and the values of the (constant) integral capacities are given by in Table 1.

We use $\Gamma_s^0 = 5.7$ sites nm^{-2} (Daigle, 2021) and the values of K_p, K_d, K_{HO}, and K_{Na} given by Kallay et al. (2003) and Daigle (2021) to calculate the values of φ_d, Q_s^0 and Σ_{iw} at different concentrations based on the Equations 10 and 16–19.

2.2. REV Scale

The electrical conductivity at the macroscale is obtained by considering the cubic REV of the frozen porous media with the REV length L_0 and the corresponding cross-section area A_{REV}. We assume that the pores are circular capillary tubes whose radii varies from r_{min} to r_{max}. In addition, we assume that the PSD $f(r)$ (PSD) in the REV consists of the number of capillary tubes (radius from r to $r + dr$ as $f(r)dr$). Note that we can obtain the PSD of REV by using the hydrodynamic characteristic curves such as the water retention (capillary head-saturation) or hydraulic conductivity (relative permeability-saturation) relationships (e.g., Jougnot et al., 2012).

The conductance (Σ) of the frozen saturated REV is deduced as follows,

$$\Sigma = \int \frac{1}{R(r)} f(r)dr = \int_{r_{min}}^{r_i} \frac{1}{R_1} f(r)dr + \int_{r_i}^{r_{max}} \frac{1}{R_2} f(r)dr. \tag{20}$$

We define the electrical conductivity σ (S/m) at the REV scale by dividing the conductance with a geometric factor $f_g = \frac{\pi R^2}{L_0} = \frac{A_{REV}}{L_0}$ (Rembert et al., 2020),

$$\sigma = \frac{\Sigma}{f_g} = \int_{r_{min}}^{r_i} \frac{\pi r^2 \sigma_w}{\tau A_{REV}} f(r)dr + \int_{r_{min}}^{r_{max}} \frac{2\pi r \Sigma_{sw}}{\tau A_{REV}} f(r)dr + \int_{r_i}^{r_{max}} \frac{2\pi r \Sigma_{iw}}{\tau A_{REV}} f(r)dr, \tag{21}$$

where τ is the tortuosity at the REV scale, and we consider a constant tortuous length L_e for different size pores, so the tortuosity τ is also a constant value for different capillary radius and is defined as,

$$\tau = \frac{L_e}{L_0}. \tag{22}$$

We can safely neglect the electrical conductivities of the ice column and the mineral grains, but surface conductivity in the electrical double-layer of the grains and ice column can be significant (e.g., Coperey, Revil, Abdulsamad, et al., 2019; Daigle, 2021; Revil, 2013; Revil & Glover, 1997). As the temperature decreases, the connectivity of bulk conduction declines due to the liquid water transitions, and the decreases in the liquid water saturation (S_u) also affects the bulk conduction. As a result, the electrical conductivity (σ, S/m) in the REV is obtained using a modified Archie model for frozen media and an empirical parameter known as an unfrozen exponent (Coperey, Revil, Abdulsamad, et al., 2019; Waxman & Smits, 1968):

$$\sigma = S_u^n \int_{r_{min}}^{r_{max}} \frac{\pi r^2 \sigma_w}{\tau A_{REV}} f(r)dr + \int_{r_{min}}^{r_{max}} \frac{2\pi r \Sigma_{sw}}{\tau A_{REV}} f(r)dr + \int_{r_i}^{r_{max}} \frac{2\pi r \Sigma_{iw}}{\tau A_{REV}} f(r)dr. \tag{23}$$

where n is an empirical parameter analogous to the so-called saturation exponent, but that we hereafter call the unfrozen exponent and S_u is liquid water saturation. In this study, we are interested in the effect of two different PSDs: the (a) lognormal and the (b) fractal distributions. However, one should note that the Equation 23 can be used for any PSD $f(r)$ (see discussion in Vinogradov et al., 2021).

2.2.1. Lognormal Distribution

Porous media often exhibit a lognormal PSD (e.g., Kosugi, 1994) that can be given by

$$f(r) = \frac{A}{\sqrt{2\pi}sr}\exp\left\{-\left[\frac{\ln\left(\frac{r}{r_m}\right)}{\sqrt{2}s}\right]^2\right\}, r_{min} \leq r \leq r_{max} \tag{24}$$

where r_m represents the geometric mean pore radius (in m), A is a normalizing prefactor, and s represents the log-normal standard deviation. Therefore, we can calculate the total capillaries number (N) with following the lognormal distribution in the REV scale

$$N = \int_{r_{min}}^{r_{max}} f(r)\mathrm{d}r = \int_{r_{min}}^{r_{max}} \frac{A}{\sqrt{2\pi}sr}\exp\left\{-\left[\frac{\ln\left(\frac{r}{r_m}\right)}{\sqrt{2}s}\right]^2\right\}\mathrm{d}r = \int_{\frac{\ln\left(\frac{r_{min}}{r_m}\right)}{\sqrt{2}s}}^{\frac{\ln\left(\frac{r_{max}}{r_m}\right)}{\sqrt{2}s}} \frac{A}{\sqrt{\pi}}e^{-t^2}$$

$$\mathrm{d}t = \frac{A}{2}\left[\mathrm{erf}\left(\frac{\ln\left(\frac{r_{max}}{r_m}\right)}{\sqrt{2}s}\right) - \mathrm{erf}\left(\frac{\ln\left(\frac{r_{min}}{r_m}\right)}{\sqrt{2}s}\right)\right], \tag{25}$$

with the error function $\mathrm{erf}(z) = \frac{2}{\sqrt{\pi}}\int_0^z e^{-t^2}\mathrm{d}t$.

The porosity of the REV is calculated on the basis of the lognormal distribution of capillary tubes (Jackson, 2008, 2010),

$$\phi = \frac{V_P}{V_{REV}} = \frac{\int_{r_{min}}^{r_{max}} \pi r^2 L_e f(r)\mathrm{d}r}{A_{REV}L_0} = \frac{\tau\pi}{A_{REV}}\int_{r_{min}}^{r_{max}} r^2 f(r)\mathrm{d}r, \tag{26}$$

where V_p is the total pore volume (in m³), V_{REV} is the total volume of the REV (in m³), L_e is the tortuous length of the capillary (in m), L_0 is the length of the REV (in m). Then the cross-section area that is perpendicular to the capillary tubes can be obtained:

$$A_{REV} = \frac{\tau\pi}{\phi}\int_{r_{min}}^{r_{max}} r^2 f(r)\mathrm{d}r, \tag{27}$$

where

$$\int_{r_{min}}^{r_{max}} r^2 f(r)\mathrm{d}r = \int_{r_{min}}^{r_{max}} r\frac{A}{\sqrt{2\pi}s}\exp\left\{-\left[\frac{\ln\left(\frac{r}{r_m}\right)}{\sqrt{2}s}\right]^2\right\}\mathrm{d}r = \frac{A}{\sqrt{2\pi}s}\int_{r_{min}}^{r_{max}} r\exp\left\{-\left[\frac{\ln\left(\frac{r}{r_m}\right)}{\sqrt{2}s}\right]^2\right\}$$

$$\mathrm{d}r = \frac{A}{2}r_m^2 e^{2s^2}\left[\mathrm{erf}\left(\frac{\ln\left(\frac{r_{max}}{r_m}\right) - 2s^2}{\sqrt{2}s}\right) - \mathrm{erf}\left(\frac{\ln\left(\frac{r_{min}}{r_m}\right) - 2s^2}{\sqrt{2}s}\right)\right]. \tag{28}$$

Similarly, substituting Equation 24 into Equation 23, we obtain the electrical conductivity of the frozen saturated REV with the lognormal distribution as:

$$
\sigma = S_u^n \int_{r_{\min}}^{r_{\max}} \frac{\pi r^2 \sigma_w}{\tau A_{\mathrm{REV}}} \left(\frac{A}{\sqrt{2\pi}sr} \exp\left\{ -\left[\frac{\ln\left(\frac{r}{r_{\mathrm{m}}}\right)}{\sqrt{2}s} \right]^2 \right\} \right) \mathrm{d}r + \int_{r_{\min}}^{r_{\max}} \frac{2\pi r \Sigma_{sw}}{\tau A_{\mathrm{REV}}} \left(\frac{A}{\sqrt{2\pi}sr} \exp\left\{ -\left[\frac{\ln\left(\frac{r}{r_{\mathrm{m}}}\right)}{\sqrt{2}s} \right]^2 \right\} \right) \mathrm{d}r
$$
$$
+ \int_{r_i}^{r_{\max}} \frac{2\pi r \Sigma_{iw}}{\tau A_{\mathrm{REV}}} \left(\frac{A}{\sqrt{2\pi}sr} \exp\left\{ -\left[\frac{\ln\left(\frac{r}{r_{\mathrm{m}}}\right)}{\sqrt{2}s} \right]^2 \right\} \right) \mathrm{d}r. \tag{29}
$$

Consequently, defining α as the ratio of the minimum pore radius to the maximum pore radius ($\alpha = r_{\min}/r_{\max}$), from Equations 26–29, we can obtain the electrical conductivity of saturated frozen REV:

$$
\sigma = \frac{\phi S_u^n}{\tau^2} \sigma_w + \frac{2\phi}{\tau^2} \frac{1}{r_{\mathrm{m}}} e^{-\frac{3s^2}{2}} \frac{\left(\mathrm{erf}\left(\frac{\ln\left(\frac{r_{\max}}{r_{\mathrm{m}}}\right) - s^2}{\sqrt{2}s} \right) - \mathrm{erf}\left(\frac{\ln\left(\frac{\alpha \cdot r_{\max}}{r_{\mathrm{m}}}\right) - s^2}{\sqrt{2}s} \right) \right)}{\left(\mathrm{erf}\left(\frac{\ln\left(\frac{r_{\max}}{r_{\mathrm{m}}}\right) - 2s^2}{\sqrt{2}s} \right) - \mathrm{erf}\left(\frac{\ln\left(\frac{\alpha \cdot r_{\max}}{r_{\mathrm{m}}}\right) - 2s^2}{\sqrt{2}s} \right) \right)} \Sigma_{sw}
$$
$$
+ \frac{2\phi}{\tau^2} \frac{1}{r_{\mathrm{m}}} e^{-\frac{3s^2}{2}} \frac{\left(\mathrm{erf}\left(\frac{\ln\left(\frac{r_{\max}}{r_{\mathrm{m}}}\right) - s^2}{\sqrt{2}s} \right) - \mathrm{erf}\left(\frac{\ln\left(\frac{r_i}{r_{\mathrm{m}}}\right) - s^2}{\sqrt{2}s} \right) \right)}{\left(\mathrm{erf}\left(\frac{\ln\left(\frac{r_{\max}}{r_{\mathrm{m}}}\right) - 2s^2}{\sqrt{2}s} \right) - \mathrm{erf}\left(\frac{\ln\left(\frac{\alpha \cdot r_{\max}}{r_{\mathrm{m}}}\right) - 2s^2}{\sqrt{2}s} \right) \right)} \Sigma_{iw}, \tag{30}
$$

The above theoretical model based on the lognormal distribution shows that the electrical conductivity at frost state is related not only to the liquid water saturation (S_u), but also to the porosity (ϕ), the tortuosity (τ), the maximum pore radius ($r_{\max}$), the ratio of the minimum pore radius to the maximum pore radius (α), the geometric mean pore radius (r_{m}), the log-normal standard deviation (s), the pore fluid conductivity (σ_w) and the specific surface conductance (Σ_{sw}, Σ_{iw}). To estimate the electrical conductivity σ from Equation 30 below the freezing point, the parameters ϕ, S_u, τ, $r_{\max}$, r_{m}, α and s must be known. Besides, the relationship between the parameters S_u, τ, σ_w, Σ_{sw}, Σ_{iw} and the temperature T need to be calculated.

2.2.2. Fractal Distribution

Another frequently encountered PSD is the fractal PSD (e.g., Tyler & Wheatcraft, 1990; Yu & Cheng, 2002):

$$
N(\geq r) = \left(\frac{r_{\max}}{r} \right)^{D_{\mathrm{f}}}, \tag{31}
$$

where $N(\geq r)$ is the number of the capillaries (with radius larger than r) in the fractal porous medium, $r_{\max}$ represents the maximum radius of capillary in the REV (in m), D_{f} represents the fractal dimension, which is between 1 and 2 for a two-dimensional pore space as well as between 2 and 3 for a three dimensional pore space.

Differentiating Equation 31 with respect to r yields

$$
-\mathrm{d}N = D_{\mathrm{f}} r_{\max}^{D_{\mathrm{f}}} r^{-D_{\mathrm{f}}-1} \, \mathrm{d}r, \tag{32}
$$

where $-\mathrm{d}N$ represents the number of pores with radius from r to $r + \mathrm{d}r$. The sign $(-)$ in Equation 32 means that the number of pores declines with increasing pore radius (Yu & Cheng, 2002; Yu et al., 2001). Therefore, the fractal distribution of capillary tubes is given on the basis of Equation 32:

$$f(r) = D_{\mathrm{f}} r_{\max}^{D_{\mathrm{f}}} r^{-D_{\mathrm{f}}-1}. \tag{33}$$

Therefore the total number (N) of capillaries (fractal distribution) in the REV is given by

$$N = \int_{r_{\min}}^{r_{\max}} f(r)\mathrm{d}r = \int_{r_{\min}}^{r_{\max}} D_{\mathrm{f}} r_{\max}^{D_{\mathrm{f}}} r^{-D_{\mathrm{f}}-1}\mathrm{d}r = \left(\frac{r_{\max}}{r_{\min}}\right)^{D_{\mathrm{f}}} - 1 \approx \left(\frac{r_{\max}}{r_{\min}}\right)^{D_{\mathrm{f}}}. \tag{34}$$

Here, we consider that $r_{\max} \gg r_{\min}$, that is, $\left(\frac{r_{\max}}{r_{\min}}\right)^{D_{\mathrm{f}}}$ is much larger than 1, which is normally valid in porous media.

The porosity of REV is calculated on the basis of the fractal theory,

$$\phi = \frac{V_{\mathrm{p}}}{V_{\mathrm{REV}}} = \frac{\int_{r_{\min}}^{r_{\max}} \pi r^2 L_e f(r)\mathrm{d}r}{A_{\mathrm{REV}} L_0} = \frac{\pi \tau D_{\mathrm{f}} r_{\max}^2 \left[1 - \alpha^{2-D_{\mathrm{f}}}\right]}{(2 - D_f) A_{\mathrm{REV}}}. \tag{35}$$

Then, the cross-section area that is perpendicular to capillary tubes can be obtained,

$$A_{\mathrm{REV}} = \frac{\pi \tau D_{\mathrm{f}} r_{\max}^2 \left[1 - \alpha^{2-D_{\mathrm{f}}}\right]}{(2 - D_{\mathrm{f}})\phi}. \tag{36}$$

Combining Equations 23 and 33, the following is obtained

$$\sigma = S_u^n \int_{r_{\min}}^{r_{\max}} \frac{\pi r^2 \sigma_w}{\tau A_{\mathrm{REV}}} D_{\mathrm{f}} r_{\max}^{D_{\mathrm{f}}} r^{-D_{\mathrm{f}}-1}\mathrm{d}r + \int_{r_{\min}}^{r_{\max}} \frac{2\pi r \Sigma_{sw}}{\tau A_{\mathrm{REV}}} D_{\mathrm{f}} r_{\max}^{D_{\mathrm{f}}} r^{-D_{\mathrm{f}}-1}\mathrm{d}r + \int_{r_i}^{r_{\max}} \frac{2\pi r \Sigma_{iw}}{\tau A_{\mathrm{REV}}} D_{\mathrm{f}} r_{\max}^{D_{\mathrm{f}}} r^{-D_{\mathrm{f}}-1}\mathrm{d}r. \tag{37}$$

Consequently, we can obtain the electrical conductivity of saturated frozen REV from Equations 34–37,

$$\sigma = \frac{\phi S_u^n}{\tau^2}\sigma_w + \frac{2\phi(2 - D_{\mathrm{f}})\left\{1 - \alpha^{1-D_{\mathrm{f}}}\right\}}{\tau^2(1 - D_{\mathrm{f}})r_{\max}(1 - \alpha^{2-D_{\mathrm{f}}})}\Sigma_{sw} + \frac{2\phi(2 - D_{\mathrm{f}})\left(r_{\max}^{1-D_{\mathrm{f}}} - r_i^{1-D_{\mathrm{f}}}\right)}{\tau^2(1 - D_{\mathrm{f}})r_{\max}^{2-D_{\mathrm{f}}}(1 - \alpha^{2-D_{\mathrm{f}}})}\Sigma_{iw}. \tag{38}$$

The above theoretical model based on the fractal distribution shows that the electrical conductivity below freezing temperature is linked not only with the liquid water saturation (S_u), but also with the porosity (ϕ), the tortuosity (τ), the fractal dimension (D_{f}), the maximum pore radius ($r_{\max}$), the ratio of the minimum pore radius to the maximum pore radius (α), the pore water conductivity (σ_w) and the specific surface conductance (Σ_{sw}, Σ_{iw}). To estimate the electrical conductivity σ from Equation 38 below the freezing point, the parameters of ϕ, S_u, τ, $r_{\max}$, D_{f}, and α must be known. In addition, the variation of S_u, τ, σ_w, Σ_{sw}, and Σ_{iw} with temperature T must be determined.

For saturated porous media, an empirical relationship proposed by Winsauer et al. (1952) relates the formation factor (F), the tortuosity (τ) and the porosity (ϕ), which for our study can be expressed as:

$$F = \lim_{\substack{\sigma_s \to 0, \\ S_u = 1}} \left(\frac{\sigma_w}{\sigma}\right) = \frac{\tau^2}{\phi}. \tag{39}$$

When the temperature drops, the liquid water saturation of porous media decreases gradually, and the formation of ice in the pores changes the tortuosity in the REV. At this time, considering the variation of the pore water conductivity with ionic concentration (Coperey, Revil, Abdulsamad, et al., 2019), the effective formation factor in the porous medium is

$$F_{\text{eff}} = \lim_{\sigma_s \to 0}\left(\frac{\sigma_w}{\sigma}\right) = \frac{\tau^2(T)}{\phi}(S_u(T))^{1-n}. \tag{40}$$

The derivation results (Equations 30 and 38–40) show that the electrical conductivity and the formation factor in frozen porous media are not only influenced by the liquid water saturation, which is strongly associated with the PSD of the porous medium, but also correlated with the tortuosity.

To describe the SFCC, from the freezing temperature T_0 to lower temperatures, we ignore the residual liquid water and adsorbed liquid water contents in saturated frozen porous media and use the following equation (C. Wang et al., 2017),

$$S_u = \left\{\frac{1}{\ln\left[e + \left(\frac{e^{T_0-T}}{a}\right)^b\right]}\right\}^c, \tag{41}$$

where a, b, and c are fitting parameters with values related to the pore volume fraction and the freezing temperature of the REV.

The tortuosity as a function of porosity is assessed using the following relationship established for positive temperature (e.g., Comiti & Renaud, 1989),

$$\tau(\phi) = 1 + 0.41\ln\left(\frac{1}{\phi}\right). \tag{42}$$

When the temperature decreases below the freezing temperature, the liquid water changes into ice. From Equation 42, the tortuosity then becomes (Teng et al., 2021):

$$\tau = \tau(S_u\phi) = 1 + 0.41\ln\left(\frac{1}{S_u\phi}\right). \tag{43}$$

Porosity can be obtained by experimental measurements. Due to the heterogeneity of the capillaries (an unfrozen exponent n is introduced at freezing temperature in Equation 23), the proposed model can be applied to predict the electrical conductivity of saturated frozen porous medium below the freezing temperature. Therefore, in the proposed model based on lognormal distribution, the theoretical values of the electrical conductivity in saturated frozen porous media can be calculated once the parameters of porous medium s, r_m, $r_{\max}$, α, and n are defined. In the proposed model based on fractal distribution, the theoretical values of the electrical conductivity in saturated frozen porous media can be calculated once the parameters of the porous medium D_f, $r_{\max}$, α, and n are defined.

3. Laboratory Experiments

3.1. Experimental Setup

There are two methods to measure the electrical conductivity of a sample: the two-electrode method and the four-electrode method. However, the physical properties such as electrical conductivity and liquid water saturation of frozen porous media are easily destroyed by external factors during the measurement. Therefore, to decrease the disturbance of the soil sample, the electrical conductivity measurements presented here were carried out with the two-electrode method. A schematic diagram of the instrumentation is described in Figure 3, including a sample temperature control device, an electrical conductivity measurement device and temperature measurement instrument. By adjusting the temperature of the sample and measuring the electrical resistance of the soil sample at various temperatures, the electrical conductivity of the frozen porous media can be determined through the following equation:

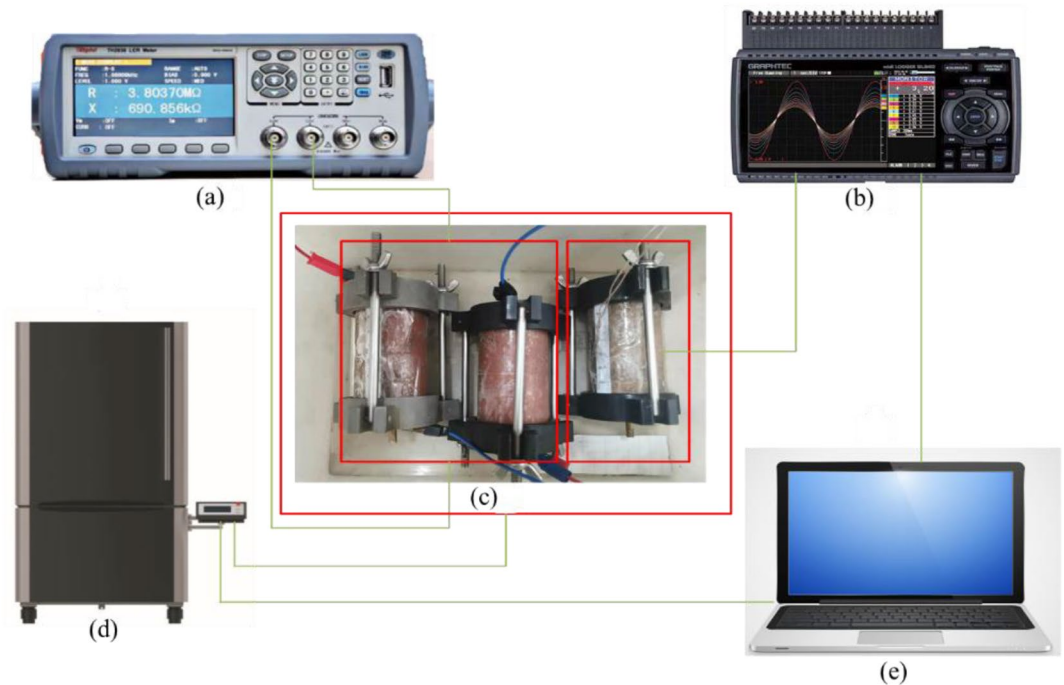$$\sigma = \frac{L}{RS} = \frac{1}{K_g R}, \tag{44}$$

Figure 3. Schematic diagram of the experimental apparatus, which consists of a temperature control system and a measurement system. The temperature control system is composed of a high and low temperature experimental chamber (d), and the measurement system includes the temperature measurement (b) and the resistance measurement of the sample (a). Soil column (c) includes the resistance sample that measures the resistance of soil sample, and the temperature sample to monitor the change of the internal temperature of sample.

where σ is the electrical conductivity of the porous media (S/m); R is the resistance (Ω); L is the length of the sample (m), and S is the area of the sample (m²). The geometrical factor $K_g = S/L$ (m) is calculated from the geometrical dimensions of the samples.

3.2. Samples and Procedures

Three kinds of soil samples are tested in the experiments including quartz sand, clay and silty soil (grain diameter lower than 2 mm) and aimed to characterize the dependence of their electrical conductivity with respect to temperature and ionic concentration. A commercial medium-coarse grained sand is selected as a material (quartz sand) that particle sizes ranges from 0.5 to 1 mm. The clay is a typical red clay sampled from Changsha (China), and the silty soil as a type of clayey silt was collected at Beijing (China). The basic properties of the three soils are listed in Table 2.

The instruments include a high- and low-temperature chamber, a high-precision LCR digital bridge, a temperature measurement device, electrodes and several electrode wires. The high- and low-temperature chamber provides a test range from 40°C to −30°C with an accuracy of 0.1°C. The electrical conductivity measurement device is a high-precision LCR digital bridge with an accuracy of 10^{-4} Ω, and a frequency range from 50 Hz to 100 kHz.

Table 2
Properties of the Samples: Quartz Sand, Silty Soil, and Clay

Sample	Liquid limit	Plastic limit	Optimum liquid water content	Maximum dry density (g/cm³)	Specific gravity	Porosity (ϕ)
Clay	36.02%	21.5%	16.2%	1.73	2.73	0.40
Silty soil	29.9%	21.5%	16.2%	1.71	2.70	0.368
Quartz sand	–	–	–	1.60	2.64	0.240
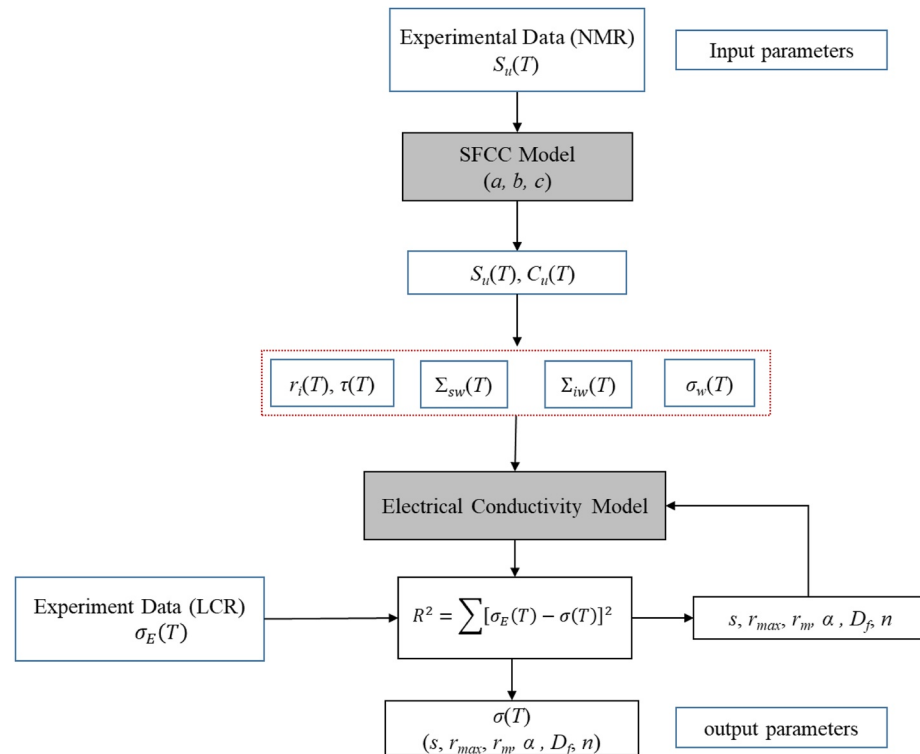
Figure 4. The flow chart to determine the electrical conductivity σ as a function of temperature from S_u, C_u, σ_w, r_i, τ, Σ_{sw}, Σ_{iw} as well as ϕ, and the microstructural parameters of the porous medium (a, b, c, s, r_{max}, r_m, α, D_f, n), where σ_E is the experimental data of electrical conductivity at freezing temperature.

A frequency of 100 Hz is adopted in this study (e.g., Abu-Hassanein et al., 1996; Coperey, Revil, Abdulsamad, et al., 2019; Kemna et al., 2014; Suits et al., 2002) to reduce the influence of high-frequency ice polarization and low-frequency electrode polarization phenomena. The temperature measurement device has a test accuracy of 0.1°C. A triaxial sample cavity (90 mm height and 40 mm diameter) is adopted for sample loading. To eliminate the influence of metallic materials on the conductivity of the sample, the metallic parts of the triaxial cavity were replaced by plexiglass parts. Copper electrode plates with a diameter of 40 mm and a height of 2 mm are applied in addition to a set of copper wires.

The soil samples were first washed with distilled liquid water to remove mineral ions from the soil pores, and then were dried during 24 hr at about 75°C. Then, the samples were mixed with sodium chloride solution at different concentrations to achieve different initial ionic concentrations. Each sample was compacted into a container at the required dry density, and then saturated under vacuum with the same solutions. At the end of the saturation process, a 2 mm graphite powder layer was placed at both ends of the sample to reduce the impact of contact resistance. Copper electrode plates were then placed at both ends of the soil sample, and the whole was placed in a temperature control chamber. Corresponding sample was prepared under the same condition and used to monitor the change of the internal temperature of sample and to measure the liquid water saturation at corresponding temperature. The temperature range was −20°C to 25°C. When the sample temperature became constant, the value of the electrical resistance was recorded at this temperature, thus the electrical conductivity was determined. The results of experiments are summarized in Appendix A, including the values of liquid water saturation and electrical conductivity of frozen porous media. The freezing characteristic curve of these three soils was measured via the NMR method, which calculates the liquid water content based on the inversion results of hydrogen signal values in different states by recording the energy level of hydrogen atoms in the samples (e.g., Shen et al., 2020; Teng, Kou et al., 2020).
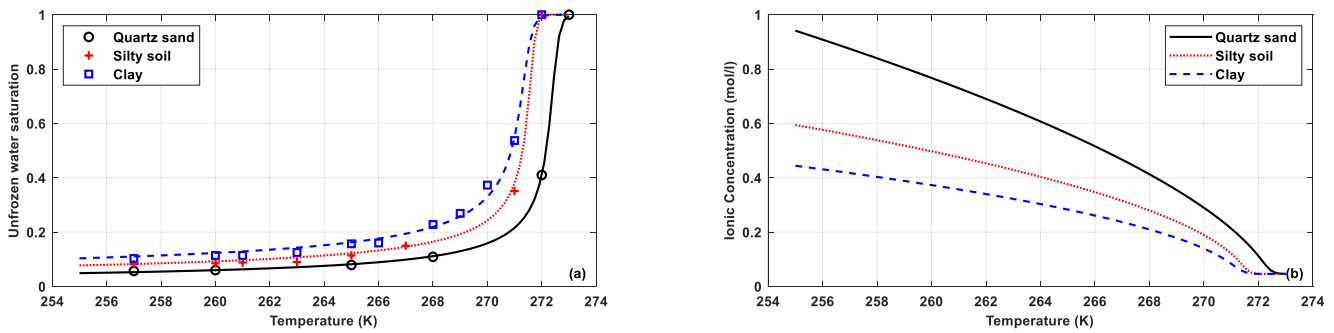
Figure 5. Liquid water saturation and ionic concentration as a function of temperature for saturated frozen porous media (quartz sand, silty soil and clay), as measured experimentally (symbols) (initial ionic concentration is 0.046 mol/L, see Table 3) and predicted by the model (lines). (a) Liquid water saturation—Equation 41: quartz sand, $a = 1.60$, $b = 8.11$, $c = 0.609$; silty soil, $a = 3.69$, $b = 10$, $c = 0.50$; clay, $a = 4.41$, $b = 6.50$, $c = 0.485$. (b) Ionic concentration—Equation 6: quartz sand, silty soil and clay.

4. Results and Discussion

4.1. Sensitivity Analysis of the Model

Under freezing temperature, the pore water in porous media gradually changes into ice. Consequently, it leads to the decrease of the liquid water saturation and the increase of ionic concentration in capillaries, which affect the pore water electrical conductivity and specific surface conductances. Besides, ice and liquid-pore solution resulting from the phase transformation of liquid water will form a new EDL that also affects the surface conduction. Finally, the formation of ice in the pore has a great influence on the tortuosity, which may largely reduce the electrical conductivity of the saturated frozen REV.

Figure 4 describes the flow procedure used to predict the value of proposed model and to perform a sensitivity analysis of our model. First, we obtained the liquid water saturation based on the SFCC (Equation 41), then the ionic concentration and the tortuosity can be determined from the known initial concentration and liquid water saturation (Equations 6 and 43) and the critical freezing radius with temperature from the Gibbs-Thomas effect (Equation 1). Second, the pore water conductivity and specific surface conductance at the solid surface-liquid water and bulk ice-liquid water interfaces are determined according to the surface complexation model. Finally, the electrical conductivity as a function of temperature with PSD in saturated frozen porous media is predicted based on Equations 30 and 38 using representative values of parameters of lognormal distribution (n, s, r_{max}, r_m, α) or of fractal distribution (n, r_{max}, α, and D_f).

To estimate the effect of the temperature on the electrical conductivity with a lognormal or fractal distribution in saturated frozen porous media based on Equations 30 and 38, the change of the liquid water saturation, of the ionic concentration as well as of the critical freezing radius with temperature on the basis of the Gibbs-Thomas effect must be determined first.
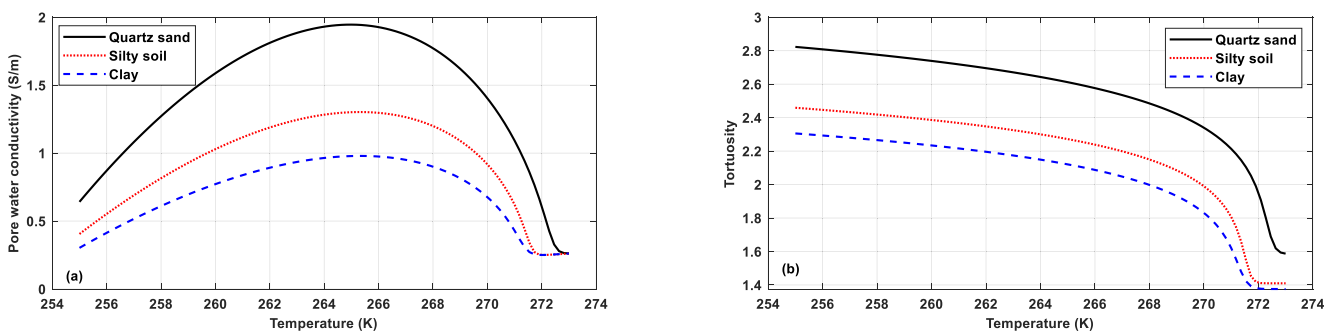

Figure 6. Variations of pore water conductivity and tortuosity as a function of temperature for different types of saturated frozen porous media (quartz sand, silty soil and clay). (a) Pore water conductivity is obtained from Equation 9 and the initial ionic concentration of electrolyte is 0.046 mol/L; (b) Tortuosity is given by Equation 43.
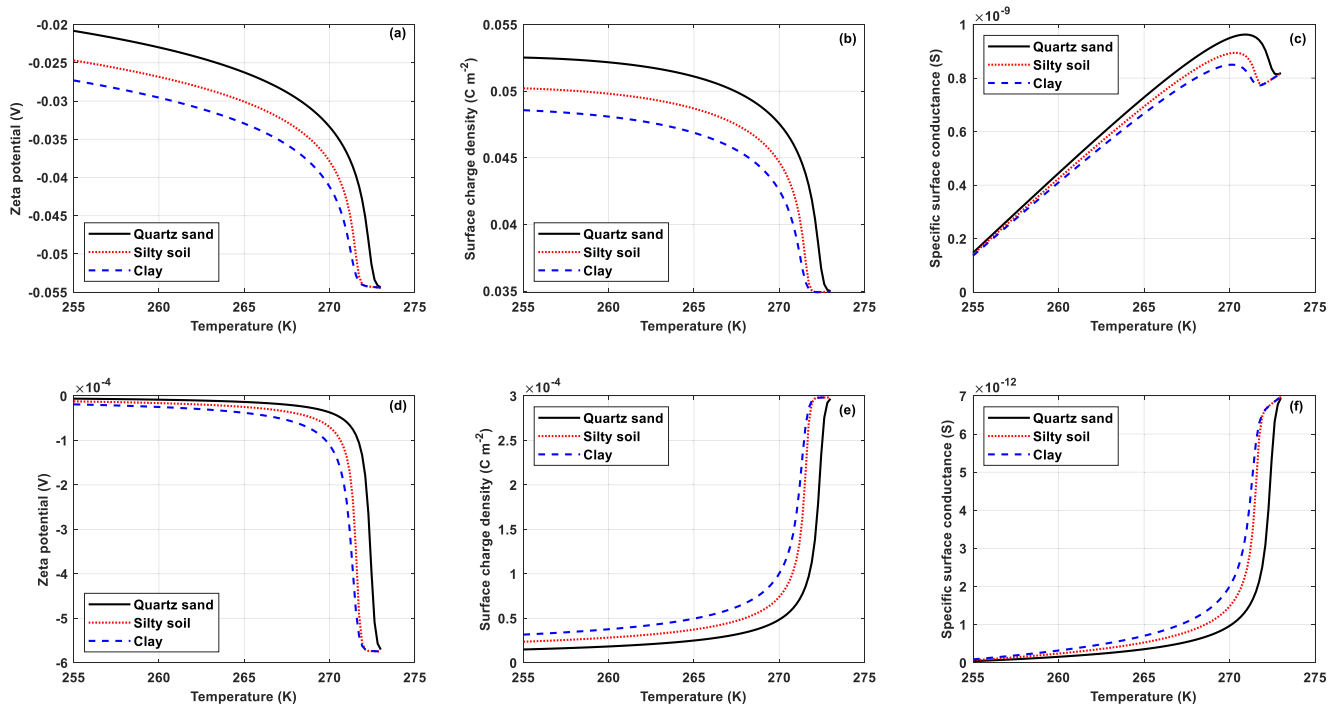
Figure 7. Variations of zeta potential, surface charge density and specific surface conductance with temperature at the solid surface-liquid water and bulk ice-liquid water interfaces. (a) Zeta potential in the interface between solid surface and liquid water; (b) Surface charge density at the electrical double layers (EDLs) in the interface between solid surface and liquid water; (c) Specific surface conductance in the interface between solid surface and liquid water; (d) Zeta potential in the interface between bulk ice and liquid water; (e) Surface charge density at the EDLs in the interface between bulk ice and liquid water; (f) Specific surface conductance in the interface between bulk ice and liquid water.

Figure 5a presents the liquid water saturation as a function of temperature for quartz sand, silty soil and clay, as obtained from our experiments (see Appendix A, initial ionic concentration 0.046 mol/L) and predicted by Equation 41. The best fits are obtained with quartz sand ($a = 1.60$, $b = 8.11$, $c = 0.609$), silty soil ($a = 3.69$, $b = 10$, $c = 0.50$) and clay ($a = 4.41$, $b = 6.50$, $c = 0.485$), and the model prediction is shown to be in very good agreement with the measured data. The continuous decrease in liquid water saturation with decreasing temperature can be divided into two stages for the three soils: a stage of strong decline followed by a stage of slight decrease. For a bundle composed predominantly of large capillaries like quartz sand, the liquid water saturation drops sharply near the freezing temperature of bulk liquid water ($T_0 = 273.15$ K), and then, the slope of the SFCC gradually decrease as the ratio of capillaries with small radius to large radius in the bundle increases. For soils with a smaller capillary radius, such as clay and silty soil, there is a lower SFCC turning point temperature. This is because a smaller capillary radius corresponds to a higher matric suction in the soil, that is, the liquid water should more difficult to change into ice, thus the freezing temperature of the bulk liquid water is lower for saturated porous medium, and the amount of liquid water content remains higher than in soils with larger capillaries.

The variation of ionic concentration as a function of temperature for saturated frozen porous media is depicted in Figure 5b and the predicted model is given by Equation 6. The ionic concentration is related to the initial concentration and liquid water saturation, and goes up with decreasing temperature.

It can be seen from the model that the electrical conductivity of the frozen soils relies on the pore water conductivity and on the tortuosity. Consequently, we evaluate the evolution of these parameters with the changes of temperature from Equations 9 and 43. Figure 6a illustrates the sensitivity of the pore water conductivity to temperature: it first increases with a decrease in temperature near the freezing temperature before decreasing. This behavior is explained on the basis of Equation 9 by the variation of the temperature and the ionic concentration. On the one hand, when the temperature falls, the electrical conductivity of frozen porous medium declines because of a decreasing ionic mobility (see Equations 8 and 9). On the other hand, as the temperature decreases, the ionic concentration rises, thus the pore water conductivity increases. Note that the effect of electrolyte concentration is largest near the freezing temperature whereas that of temperature is predominant at lower temperatures due to a

maximum value of the pore water conductivity. The variation of tortuosity as a function of temperature in saturated frozen porous media is shown in Figure 6b and the predicted model is given by Equation 43. The tortuosity is linked to the porosity and liquid water saturation, and increases with the decrease of temperature.

Furthermore, the electrical conductivity of porous media in frost state associated with the specific surface conductance at the solid surface-liquid water and bulk ice-liquid water interfaces. We therefore illustrate the change in specific surface conductances with temperature at the solid surface-liquid water and bulk ice-liquid water interfaces.

The variations of the zeta potential, the surface charge density at the EDLs and the specific surface conductance of solid surface-liquid water interface with the temperature are obtained based on the surface complexation model and given in Figures 7a–7c, and we assume that the electrical potential at d-plane is equal to the zeta potential, because the two are very close to each other (e.g., Revil & Glover, 1997). The corresponding equilibrium constants of surface complexation reactions are given in Table 1. When an external electrical potential gradient (or electrical field) is applied, then some of the electrolyte in pore water and the excess charge within the EDLs including the outer sphere surface complexes in the Stern layer and diffuse layer are transported with the flow, resulting in electrical conduction and streaming currents. It is clear from Figure 7a that the calculated value of the zeta potential declines in magnitude with decreasing temperature. On the one hand, the liquid water content drops when temperature decreases, resulting in decreasing conduction and streaming currents, but the streaming current decreasing faster than the conduction current. The reason is that conduction current encompasses interfacial ion contribution, which is less sensitive to temperature than bulk ion contribution due to ion and liquid water molecule crowding (less liquid water molecules available to transform from liquid to ice, this is the source of the same effect than the effect of pore size on temperature freezing of liquid water molecules). Streaming potential current only encompasses contribution of moving ions under liquid water flow in the diffuse layer and bulk liquid water, which may be more sensitive to decreasing temperature. As the conduction current is opposed to the streaming current (see Figure 1 of Li et al., 2016), decreasing temperature below the freezing temperature may decrease the zeta potential magnitude because of an increasing effect of conduction current to the SP (Collini & Jackson, 2022; Jackson, 2010; Li et al., 2016). On the other hand, the electrolyte concentration increases with decreasing temperature, consequently the zeta potential of solid surface-liquid water interface decreases in magnitude due to the compression of the diffuse layer, consistent with published works (e.g., Jougnot et al., 2020; Pride & Morgan, 1991; Revil & Glover, 1997). The surface charge density at the EDLs has been computed from Equations 10–15. Its value is given in Figure 7b for the three different samples at pH = 7. It is observed that the surface charge density at solid surface-liquid water double layers increases when temperature decreases. The increase of the computed surface charge density of the double layers magnitude with decreasing temperature is a pure increasing salinity effect (more counter-ions in the diffuse layer compared to in bulk liquid water when the electrolyte concentration increases), in agreement with the findings of Revil & Glover (1997). In Figure 7c, we plot the specific surface conductance as a function of temperature predicted by Equation 10. When temperature is close to the freezing temperature, the specific surface conductance increases with decrease of temperature, but decreases with temperature below a certain value. Near freezing temperature and at low electrolyte concentration, the specific surface conductance is dominated by the solid diffuse layer surface charge density, which rises when temperature decreases (Figure 7b). In contrast, at lower temperature, the specific surface conductance mainly depends on the temperature due to its effect of on ion mobility (decreasing ion mobility, Equation 10), hence there is a maximum value in the curve of the variation of the specific surface conductance with temperature near the freezing temperature (Figure 7c).

The variations of the zeta potential, the surface charge density at the EDLs and the specific surface conductance of bulk ice-liquid water with the temperature are given in Figures 7d–7f. The zeta potential is assumed to be equal to the Stern electrical potential. Table 1 display the equilibrium constants used for our computations (e.g., Daigle, 2021; Kallay et al., 2003). Figure 7d shows that the zeta potential at the bulk ice-liquid water interface rapidly decreases in magnitude when the temperature drops near the freezing temperature, then the zeta potential magnitude slowly decreases. The variation of the diffuse layer surface charge density with temperature is given in Figure 7e and the result is in agreement with the results in Daigle (2021). The specific surface conductance as a function of temperature is given by Equation 10 and plotted in Figure 7f. It is seen from Figures 7e and 7f that the surface charge density and specific surface conductance of the frozen porous medium rapidly decline with decreasing temperature near freezing temperature, except when the liquid water saturation remains stable (see Figure 5a). In addition, the specific surface conductance of bulk ice-liquid water interface is one to two orders
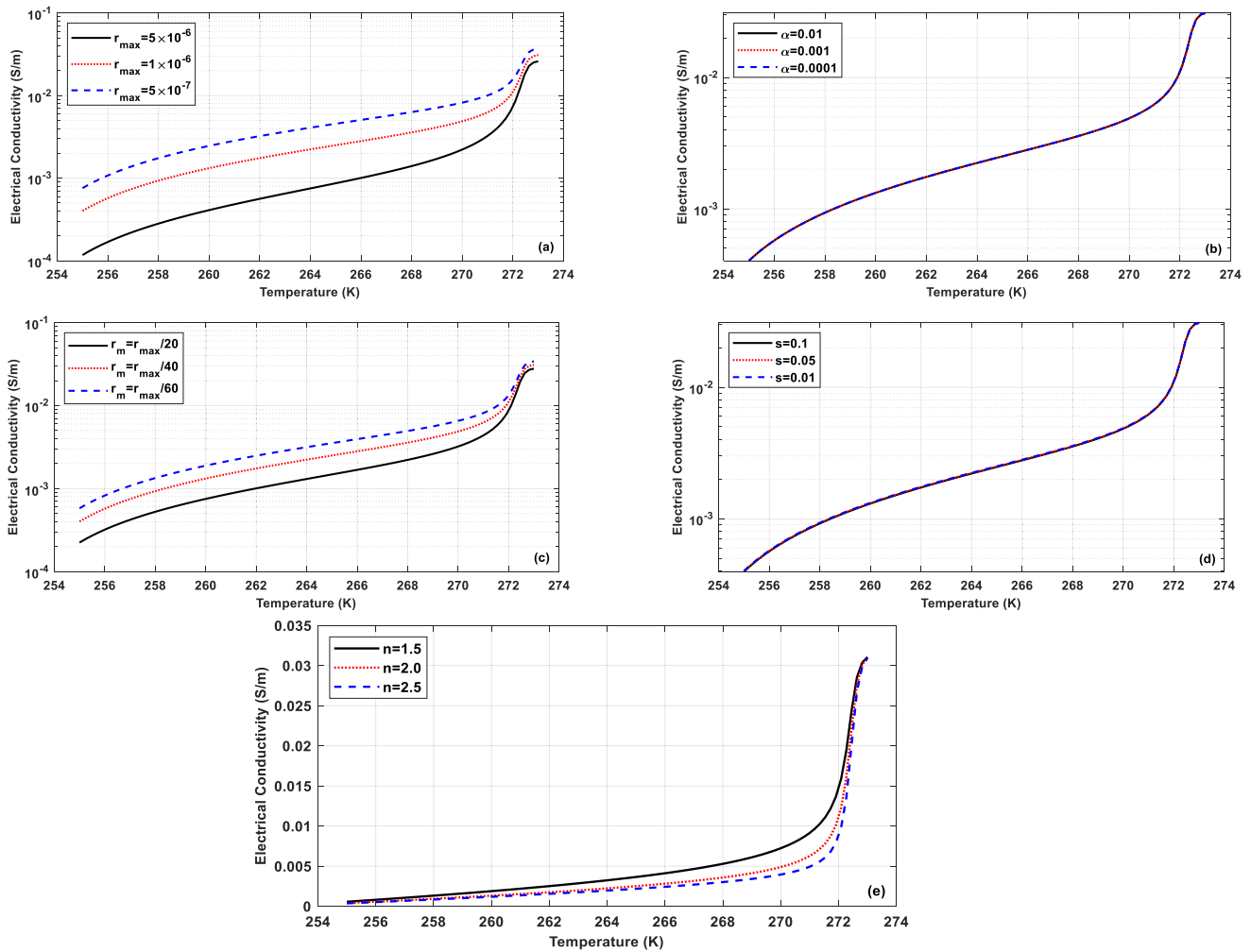
Figure 8. The dynamic electrical conductivity as a function of temperature predicted from the lognormal PSD-Equation 30, for a ionic concentration of 0.046 mol/L. (a) Effect of the maximum pore radius r_{max} on the electrical conductivity σ for three representative values of r_{max} (5×10^{-6}, 1×10^{-6}, 5×10^{-7} m); (b) Effect of the ratio α on the electrical conductivity σ for three representative values of α (0.1, 0.001, 0.0001); (c) Effect of the geometric mean pore radius r_m on the electrical conductivity σ for three representative values of r_m ($r_{max}/20$, $r_{max}/40$, $r_{max}/60$); (d) Effect of the log-normal standard deviation s on the electrical conductivity σ for three representative values of s (0.1, 0.05, 0.01); (e) Effect of the unfrozen factor n on the electrical conductivity σ for three representative values of n (1.5, 2.0, 2.5). The value of the parameters which remain constant is $r_{max} = 1 \times 10^{-6}$ m, $r_m = r_{max}/40$, s = 0.01, α = 0.005 and n = 2.0.

of magnitude lower than that of the mineral surface-liquid water interface from Figures 7c–7f, thus the surface conductivity contribution from ice/liquid water interface can be safely neglected in the case of field monitoring or inversion (Duvillard et al., 2018).

The robustness of the model for both lognormal and fractal PSDs has been tested, through a sensitivity analysis based on Equations 30 and 38. We test the effects of the maximum radius r_{max}, the ratio of the minimum pore radius to the maximum pore radius α, the geometric mean pore radius r_m, the log-normal standard deviation s, the fractal dimension D_f and the unfrozen factor n, because these parameters have significant impact on the lognormal or fractal PSDs as well as on the geometry of the porous medium.

Figure 8 shows the dynamic electrical conductivity as a function of temperature predicted from the lognormal distribution-Equation 30. In order to ignore the influence of lognormal PSD on liquid water saturation, Equation 41 is used to represent the amount of liquid water saturation in the sensitivity analysis of the model, so that only the variations of r_{max}, r_m, α, and s affect the surface conductivity of REV. The parameters of the SFCC model are $a = 1.60$, $b = 8.11$, $c = 0.609$ (quartz sand). Figures 8a and 8c show the effects of the maximum pore radius r_{max} on the electrical conductivity σ for three representative values of r_{max} (5×10^{-6}, 1×10^{-6},
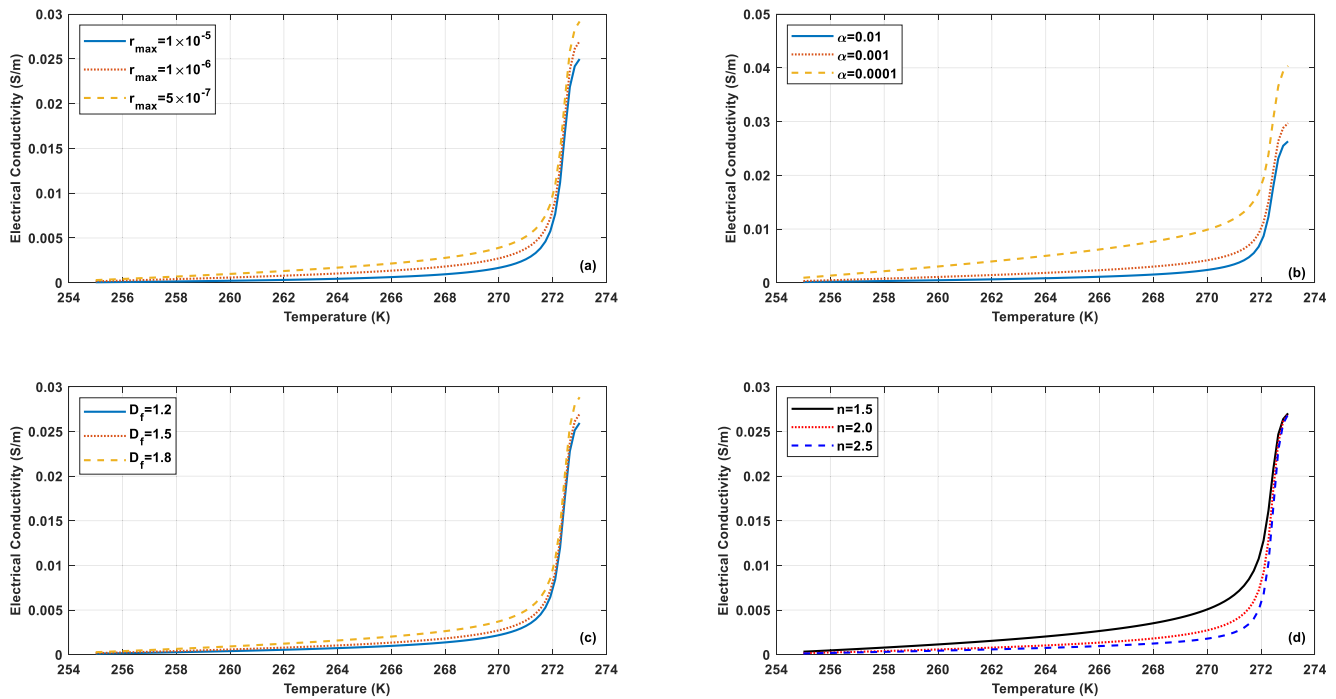
Figure 9. The dynamic electrical conductivity as a function of temperature predicted from the fractal pore size distribution-Equation 38, for a ionic concentration of 0.046 mol/L. (a) Effect of the maximum pore radius r_{max} on the electrical conductivity σ for three representative values of r_{max} (5×10^{-6}, 1×10^{-6}, 5×10^{-7} m); (b) Effect of the ratio α on the electrical conductivity σ for three representative values of α (0.1, 0.001, 0.0001); (c) Effect of the fractal dimension D_f on the electrical conductivity σ for three representative values of D_f (1.2, 1.5, 1.8); (d) Effect of the unfrozen factor n on the electrical conductivity σ for three representative values of n (1.5, 2.0, 2.5). The value of the parameters which remain constant is $r_{max} = 1 \times 10^{-6}$ m, $D_f = 1.5$, $\alpha = 0.005$ and $n = 2.0$.

5×10^{-7} m) and of the geometric mean pore radius r_m on the electrical conductivity σ for three representative value of r_m ($r_{max}/20$, $r_{max}/40$, $r_{max}/60$). They both produce significant differences in the predicted electrical conductivity, which increases with decreasing r_{max} or r_m. Indeed, when the maximum pore radius decreases, the geometric mean pore radius r_m also decreases, and the number of smaller radius capillaries increases as shown in Thanh et al. (2021) (their Figures 2b and 2e). Therefore, one can see an increase of the surface conductivity of the REV, hence an increase in electrical conductivity of the frozen porous medium. Figures 8b and 8d show the effects of the ratio of the minimum pore radius to the maximum pore radius α on the electrical conductivity σ for three representative values of α (0.1, 0.001, 0.0001) and of the log-normal standard deviation s on the electrical conductivity σ for three representative values of s (0.1, 0.05, 0.01). The electrical conductivity is not very sensitive to α and s as shown by the curves overlap for the different parameter values, although the minimum pore radius r_{min} decreases when α decreases at a fixed r_{max}. This was expected because the geometric mean pore radius (r_m) does not change, thus the number of capillaries characterized by a relatively small radius does not really increase, thus no variation is observed in the curves of electrical conductivity based on lognormal PSD (see Figures 2c and 2f in Thanh et al., 2021). In addition, Figure 8e shows the effect of the unfrozen factor n on the electrical conductivity σ for three representative values of n (1.5, 2.0, 2.5). The electrical conductivity decreases with an increase of n, because of its effect on the bulk conductivity of the porous media.

Finally, from this parametric analysis of the model with lognormal PSD, we can conclude that the electrical conductivity is highly dependent on the parameters r_{max} and r_m, which produce strong changes in PSD. Besides, the uncertainty on the unfrozen factor n produces the most significant changes in the estimates of electrical conductivity. The electrical conductivity is less sensitive to the parameters α and s.

Figure 9 presents the variation of the electrical conductivity with temperature for fractal PSD. In order to ignore the influence of fractal PSD on liquid water saturation, Equation 41 is used to represent the amount of liquid water saturation in the sensitivity analysis of the model, so the variations of r_{max}, α and D_f only influence the surface conductivity of the REV. The parameters of the SFCC model are taken as $a = 1.60$, $b = 8.11$, $c = 0.609$
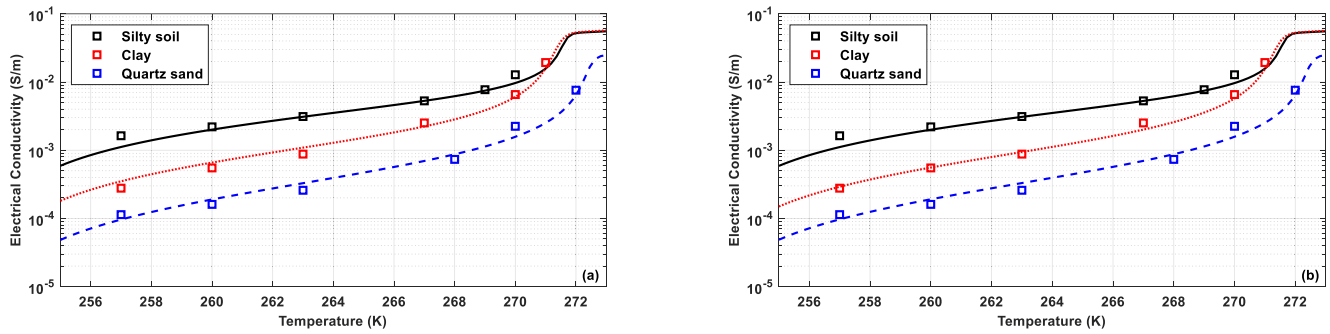
Figure 10. Electrical conductivity σ as a function of temperature for three soil samples, as measured in our experiments (symbols) and predicted by the lognormal and fractal pore size distributions (PSDs) models (solid lines). (a) Lognormal distribution, initial concentration 0.046 mol/L; (b) Fractal distribution, initial concentration 0.046 mol/L. The best fit parameters of lognormal and fractal PSDs are re-shown in Table 3.

(quartz sand). Figures 9a, b and c show the effects of the maximum pore radius r_{max} on the electrical conductivity σ for three representative values of r_{max} (5×10^{-6}, 1×10^{-6}, 5×10^{-7} m), of the ratio of the minimum pore radius to the maximum pore radius α on the electrical conductivity σ for three representative values of α (0.1, 0.001, 0.0001) and of the fractal dimension D_f on the electrical conductivity σ for three representative value of D_f (1.2, 1.5, 1.8), respectively. The electrical conductivity σ increases with the increase in D_f, or with the decrease in r_{max} or α. Indeed, when D_f increases, or when r_{max} or α decreases, the number of capillaries characterized by a relatively small radius rises, as indicated in Figures 2a and 2d in Thanh et al. (2021). Consequently, the surface conductivity of the REV elevates, thus, the electrical conductivity σ rises. Furthermore, we also observe that α has a visible influence on the electrical conductivity in fractal PSD. The reason for this phenomenon is that the electrical conductivity of the REV is mainly dominated by the geometric mean pore radius (r_m) in the lognormal distribution, while it is mainly affected by the minimum pore radius (α) in the fractal distribution. In addition, Figure 9d shows the impact of the unfrozen factor n on the electrical conductivity σ for three representative values of n (1.5, 2.0, 2.5). The electrical conductivity of porous media declines with an increase of n, as for the lognormal PSD.

Finally, from this parametric analysis of the model with fractal PSD, we illustrate that the electrical conductivity is highly sensitive to the parameters r_{max}, α and D_f, which produce strong changes in PSD. Besides, the uncertainty on the unfrozen factor n produces the most significant changes in the estimates of electrical conductivity.

4.2. Comparison With New Experimental Data

Figures 10 and 11 present the fit of the proposed model to the experimental data for the electrical conductivity in frost state as a function of the temperature by combining the SFCC model, the pore water conductivity and the specific surface conductances at the solid surface-liquid water and bulk ice-liquid water interfaces with the

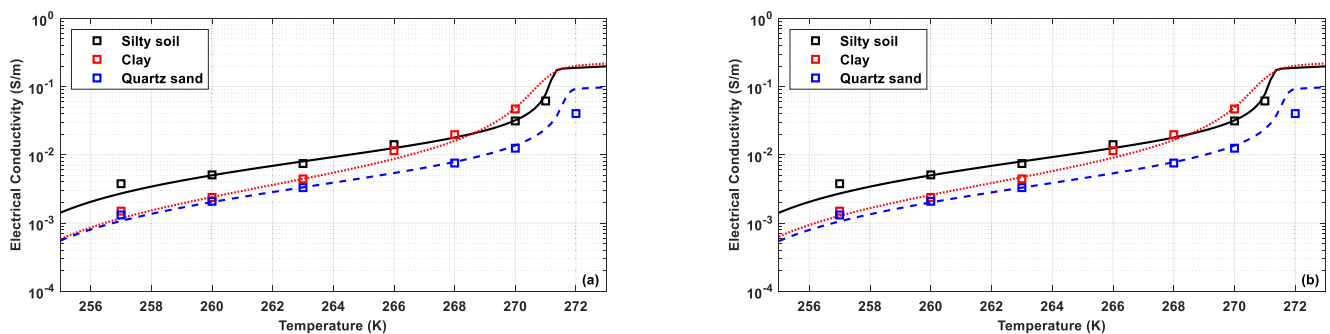**Figure 11.** Electrical conductivity σ as a function of temperature for three soil samples, as measured in our experiments (symbols) and predicted by the lognormal and fractal pore size distributions (PSDs) models (solid lines). (a) Lognormal distribution, initial concentration 0.180 mol/L; (b) Fractal distribution, initial concentration 0.180 mol/L. The best fit parameters of lognormal and fractal PSDs are re-shown in Table 3.

Table 3
The Fitting Parameters Used for Modeling and Explaining the Experimental Data

ID	ϕ	C_0 (mol/L)	a	b	c	r_{max} (m)	r_m (m)	s	α	n	D_f
Clay	0.40	0.046	4.41	6.50	0.485	3×10^{-6}	$r_{max}/15$	0.01	0.005	2.5	1.35
Clay	0.40	0.180	6.40	3.00	0.530	3×10^{-6}	$r_{max}/15$	0.01	0.005	2.5	1.70
Silty soil	0.368	0.046	3.69	10	0.50	3×10^{-6}	$r_{max}/70$	0.01	0.001	1.9	1.86
Silty soil	0.368	0.180	5.67	15.71	0.427	3×10^{-6}	$r_{max}/70$	0.01	0.001	1.9	1.85
Quartz sand	0.240	0.046	1.60	8.11	0.609	4×10^{-5}	$r_{max}/10$	0.01	0.005	1.9	1.40
Quartz sand	0.240	0.180	3.61	12	0.446	4×10^{-5}	$r_{max}/10$	0.01	0.005	1.9	1.60

Note. Parameters of the liquid water saturation model: a (no unit), b (no unit), c (no unit). Parameters of the lognormal and fractal pore size distribution models are r_m (m), r_m (m), s (no unit), α (no unit), n (no unit), and D_f (no unit).

linear model for the temperature dependence of the mobilities. Experimental data are shown by the symbols and are taken from Table 3, including the electrical conductivity data as a function of temperature. Based on the experimental data of liquid water saturation, the parameters of the SFCC model are obtained from Equation 41, and the values of the parameters are presented in Table 3. In accordance with the liquid water saturation, the ionic concentration and the specific surface conductance at the solid surface-liquid water and bulk ice-liquid water interfaces are estimated as seen in the previous sections. The fitting parameters are reported in Table 3. Two stages are observed in the electrical conductivity variation with temperature below the freezing temperature for the three different samples: a phase of rapid decline followed by a slower decline stage, which are consistent with the SFCC curve. When the temperature drops beyond the freezing temperature, the electrical conductivity of the porous medium rapidly decreases with decreasing temperature and liquid water content. When the liquid water content in the frozen state stabilizes, the conductivity slowly decreases. It appears that the liquid water saturation has a strong effect on the electrical conductivity. In addition, the fitting results illustrate the quality of the predictions of the proposed models either with lognormal or fractal PSDs, which are in very strong agreement with the experimental data, and the effect of the different PSD on the electrical conductivity will be presented in the next section.

4.3. Comparison With Published Data

4.3.1. Coperey, Revil, Abdulsamad et al. (2019), and Coperey, Revil, and Stutz (2019)

To further verify the proposed model, a comparative analysis is carried out based on the experimental works of Coperey, Revil, Abdulsamad et al. (2019), Coperey, Revil, and Stutz (2019) and Duvillard et al. (2018, 2021), which provide measured electrical conductivity data below the freezing point. Figure 12 describes the variation of electrical conductivity of the saturated frozen porous media with temperature at different initial electrolyte concentrations reported by Coperey, Revil, Abdulsamad et al. (2019), Coperey, Revil, and Stutz (2019). To verify these experimental data by the proposed models, one need to determine C_0, ϕ, S_u, σ_w, τ, Σ_{sw}, and Σ_{iw}. Values of σ_w and ϕ for those specimen are shown in Coperey, Revil, Abdulsamad et al. (2019), Coperey, Revil, and Stutz (2019) and shown in Table 4. The value of C_u can be estimated using Equation 6 and is shown in Table 4. Based on the porosity and the ionic concentration, the specific surface conductances at the solid surface-liquid water and bulk ice-liquid water interfaces are determined (Section 2.1), and we also obtain the value of tortuosity with temperature (Equation 43). In order to show that the proposed models are able to reproduce the experimental data, we empirically explore the field of fitting parameters that provide a relatively good fit. It is seen that the proposed models using lognormal or fractal PSDs predict very well the experimental data using the fitting parameters shown in Table 4.

4.3.2. Duvillard et al. (2018, 2021)

Figure 13 illustrates the variation of the electrical conductivity as a function of temperature measured by Duvillard et al. (2018, 2021) for granite and rock glacier. Values of ϕ and σ_w for those samples are reported by Duvillard et al. (2018, 2021) and shown in Table 5. The value of C_u can be estimated using Equation 6 and is shown in Table 5. The specific surface conductances at solid surface-liquid water and bulk ice-liquid water interfaces are determined as seen in the previous sections on the basis of the porosity and the ionic concentration, and we also
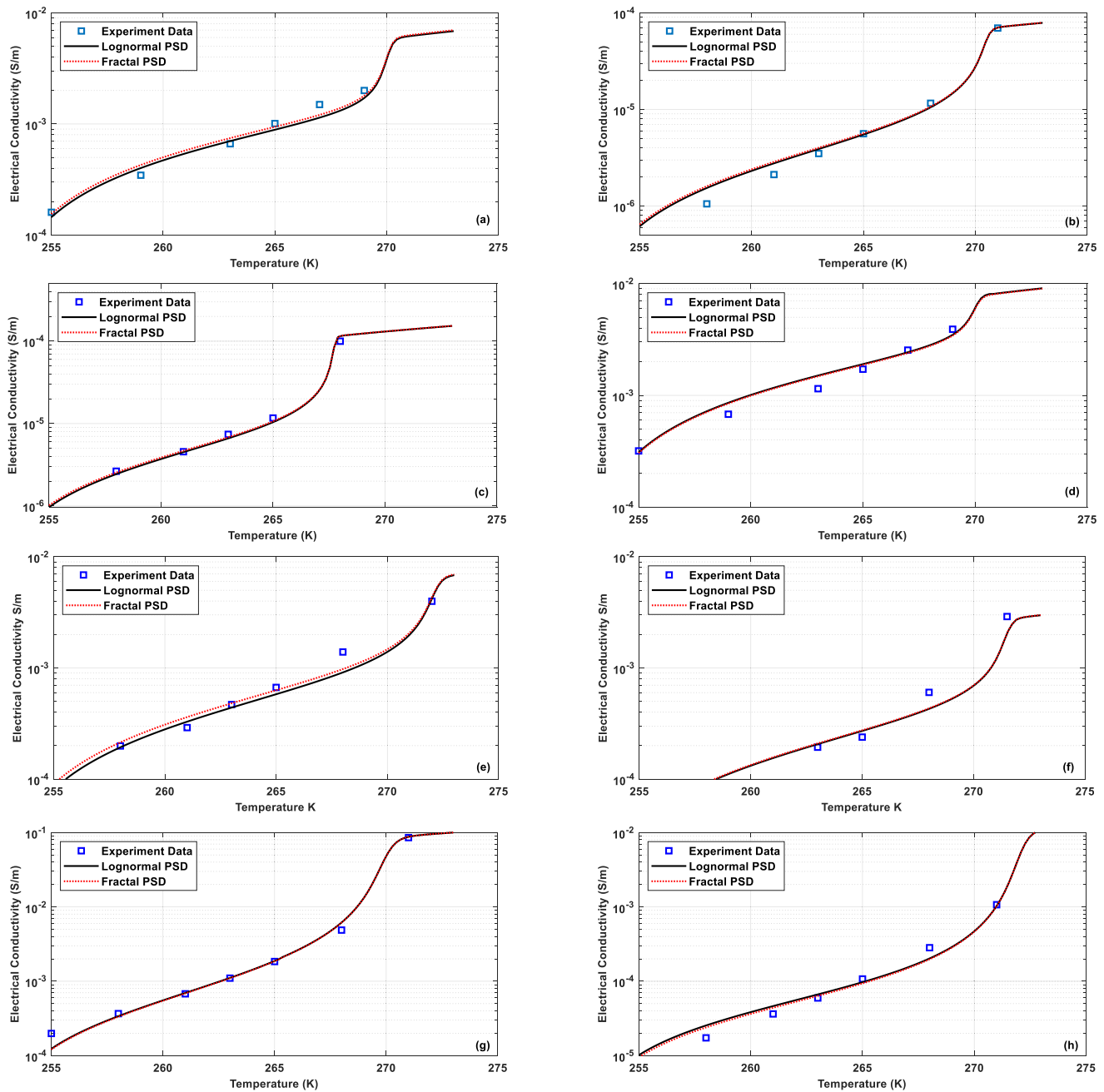
Figure 12. Electrical conductivity σ as a function of temperature. Experimental data are taken from Coperey, Revil, Abdulsamad et al. (2019), Coperey, Revil, and Stutz (2019) and the lines are predicted from Equations 30 and 38 using lognormal and fractal pore size distributions (PSDs). The best fit parameters of liquid water saturation, lognormal and fractal PSDs are shown in Table 4, separately.

obtain the value of tortuosity using Equation 43. The proposed electrical conductivity models are used to reproduce the experimental published data with the two PSDs (i.e., lognormal and fractal). They provide a fairly good match with the previously published data (fitting parameters shown in Table 5).

4.4. Formation Factor and Surface Conductivity Below Freezing Temperature

We can go one step further and compare the evolution of the bulk and surface conductivities with temperature taking advantage of the experiments presented in this work (silty soil, initial electrolyte concentration of 0.046 and 0.180 mol/L; quartz sand, initial electrolyte concentration 0.046 and 0.180 mol/L) and in Coperey, Revil,

Table 4
The Fitting Parameters Used for Proposed Models When Compared to Coperey, Revil, Abdulsamad et al. (2019), Coperey, Revil, and Stutz (2019)

Sample	ϕ	C_0 (mol/L)	a	b	c	r_{max} (m)	r_m (m)	s	α	n	D_f
(a) SW[a]	0.23	0.011	16.84	7.00	0.70	1×10^{-6}	$r_{max}/25$	0.01	0.001	1.8	1.45
(b) Granite[b]	0.028	0.0025	11	7.5	0.326	5×10^{-5}	$r_{max}/5$	0.01	0.001	2.5	1.10
(c) Granite[b]	0.052	0.0025	184.7	17.5	0.414	5×10^{-5}	$r_{max}/5$	0.01	0.005	2.0	1.10
(d) NW[a]	0.21	0.011	16.84	7.00	0.70	1×10^{-6}	$r_{max}/25$	0.01	0.001	1.5	1.58
(e) Clayey sand[b]	0.418	0.005	2.00	5.00	0.500	1×10^{-5}	$r_{max}/25$	0.01	0.001	1.8	1.50
(f) Soil[b]	0.380	0.002	4.00	6.00	0.800	2×10^{-5}	$r_{max}/30$	0.01	0.001	1.3	1.50
(g) Soil[b]	0.380	0.09	16.37	3.5	0.675	2×10^{-5}	$r_{max}/30$	0.01	0.001	2.35	1.45
(h) Soil[b]	0.380	0.01	2.049	3.9	0.722	2×10^{-5}	$r_{max}/30$	0.01	0.001	2.5	1.10

Note. Parameters of the liquid water saturation model: a (no unit), b (no unit), c (no unit). Parameters of the lognormal and fractal pore size distribution models: r_{max} (m), r_m (m), s (no unit), α (no unit), n (no unit), D_f (no unit).
[a]Coperey, Revil, and Stutz (2019), the SW and NW samples are composed of local soils and sediments with a mix of clay, silt, and gravels. [b]Coperey, Revil, Abdulsamad et al. (2019).

Abdulsamad et al. (2019), Coperey, Revil, and Stutz (2019). Figure 14 presents the variation of the electrical conductivity (bulk and surface conductivities) with the temperature, which is performed with the two samples presented in this study (silty soil and quartz sand) at different salinities. The model and experimental values of electrical conductivity are shown in Appendix A and Table 3. One can note that the bulk conductivity increases with the increase in electrolyte concentration from Figure 14a to Figure 14b and from Figure 14c to Figure 14d. Indeed, the pore water conductivity is sensitive to the salinity, thus the concentration has a strong effect on the bulk conductivity (Equations 8, 30, and 38). We also observe that the surface conductivity declines when the grain diameter rises (see from Figure 14a to Figure 14c or Figure 14b to Figure 14d). This is consistent with previous work: for the same concentration, samples with bigger particles (silty soil) have a lower specific surface than samples with smaller particles (quartz sand) (in Glover & Déry (2010) and Rembert et al. (2020)).

Figure 15 shows the variation of the electrical conductivity (bulk and surface conductivities) with the temperature for two samples measured by Coperey, Revil, Abdulsamad et al. (2019), Coperey, Revil, and Stutz (2019). The values of porosity and initial concentration are shown in Table 4. From Figure 15a, the values of the bulk conductivity are higher than those of the surface conductivity, but the surface conductivity has a higher value than the bulk conductivity from Figure 15b. This can be explained by the fact that the CEC of the NW sample (8.7 meq/100 g) has a higher value than in the granite sample (0.80 meq/100 g). As the surface conductivity is mainly sensitive to the CEC, its contribution to the total porous medium electrical conductivity is greater than the bulk conductivity (see Coperey, Revil, Abdulsamad, et al., 2019).
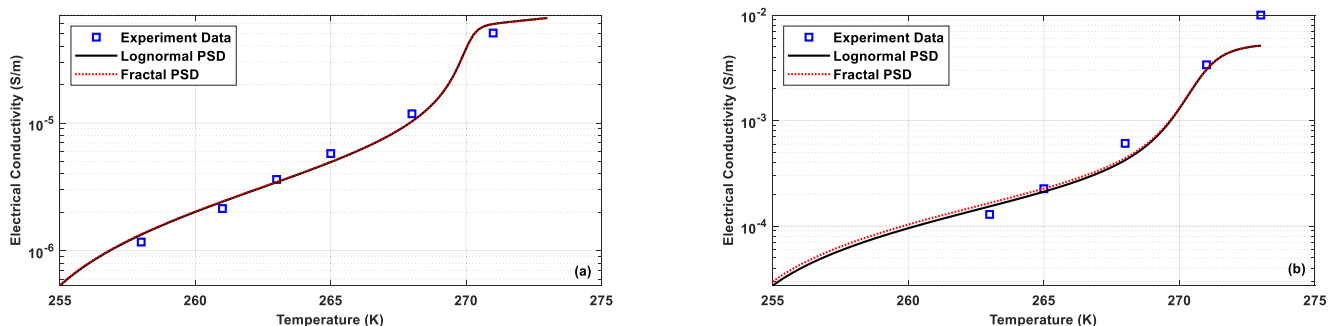

Figure 13. Electrical conductivity σ as a function of temperature. Experimental data are taken from Duvillard et al. (2018, 2021) and the lines are predicted from Equations 30 and 38 using lognormal and fractal pore size distributions (PSDs). (a) Granite, ionic concentration 0.0025 mol/L; (b) Rock glacier, ionic concentration 0.002 mol/L. The best fit parameters of liquid water saturation, lognormal and fractal PSDs are shown in Table 5, separately.

Table 5
The Fitting Parameters Used for Proposed Models When Compared to Duvillard et al. (2018, 2021)

Sample	ϕ	C_0 (mol/L)	a	b	c	r_{max} (m)	r_m (m)	s	α	n	D_f
(a) Granite[a]	0.028	0.0025	15.93	5.00	0.522	2×10^{-5}	$r_{max}/5$	0.01	0.01	2.0	1.10
(b) Rock glacier[b]	0.60	0.002	7.00	2.00	1.440	2×10^{-5}	$r_{max}/40$	0.01	0.01	1.6	1.6

Note. Parameters of the liquid water saturation model: a (no unit), b (no unit), c (no unit). Parameters of the lognormal and fractal pore size distribution model are r_{max} (m), r_m (m), s (no unit), α (no unit), n (no unit), and D_f (no unit).
[a]Duvillard et al. (2021). [b]Duvillard et al. (2018).

Figure 16 presents the evolution of the effective formation factor as a function of the temperature (experimental data from Coperey, Revil, Abdulsamad et al., 2019), which reflects the change in the liquid water content of the porous medium below the freezing temperature (fit with Equations 40, 41, and 43). From Figure 16a, the effective formation factor is constant above the freezing temperature and is independent of the electrolyte concentration, since it is only linked to the porosity and the tortuosity, see Equation 39. It sharply increases below the freezing temperature, because the effective formation factor is strongly sensitive to the liquid water saturation from Equation 40. Furthermore, we also observe that the type of samples affects the effective formation factor, which can be explained by the fact that they have various shapes and sizes and that their pore structure is extremely complex (Thanh et al., 2019). Figure 16c shows the dependence of the effective formation factor with temperature for experimental data from Coperey, Revil, Abdulsamad et al. (2019), and how the model fits the data well.

5. Conclusions

We have developed a physically-based model for the electrical conductivity dependence of temperature on the basis of the conceptualization of a porous medium using lognormal and fractal PSDs of tortuous capillary tubes. First, the electrical conductivity of a capillary tube is established based on the Gibbs-Thomson effect, considering the impact of the pore water conductivity as well as specific surface conductance at the solid surface-liquid water and bulk ice-liquid water interfaces. Then the electrical conductivity at the REV scale is obtained by means of an
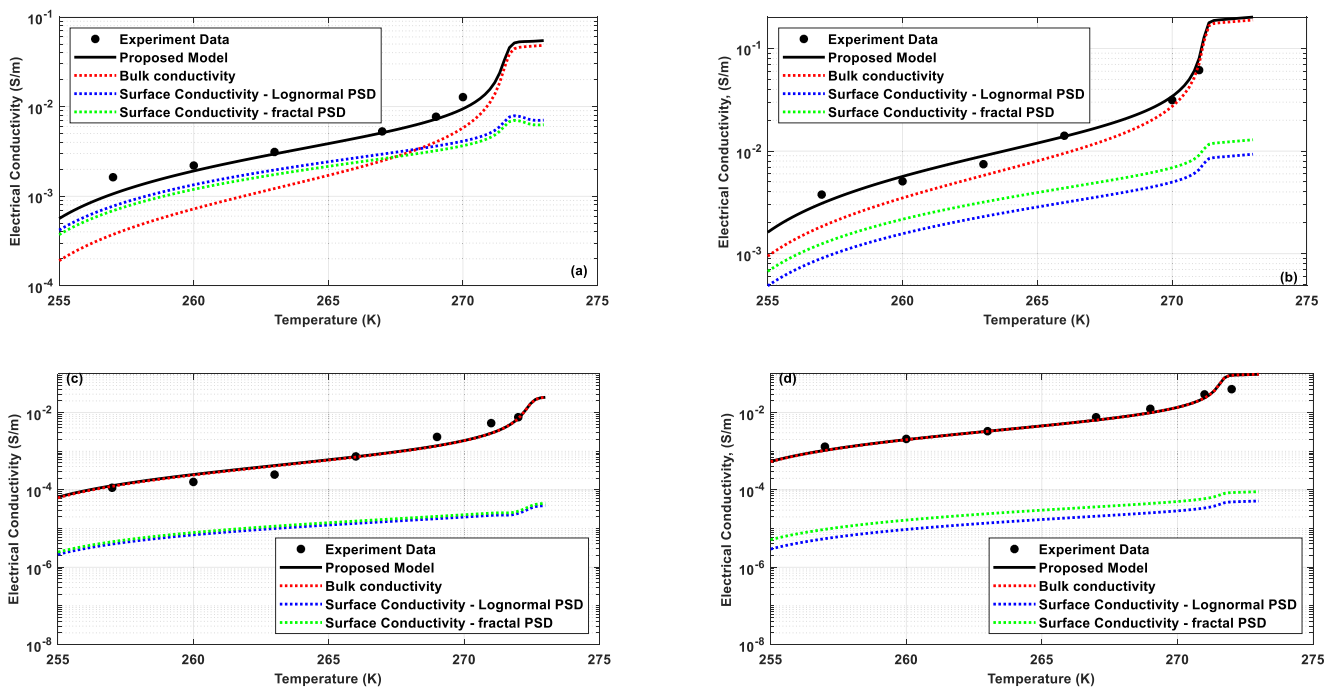

Figure 14. Evolution of the bulk conductivity and surface conductivity with temperature for lognormal and fractal pore size distributions. (a) Silty soil, initial concentration is 0.046 mol/L; (b) Silty soil, initial concentration is 0.180 mol/L; (c) Quartz sand, initial concentration is 0.046 mol/L; (d) Quartz sand, initial concentration is 0.180 mol/L.
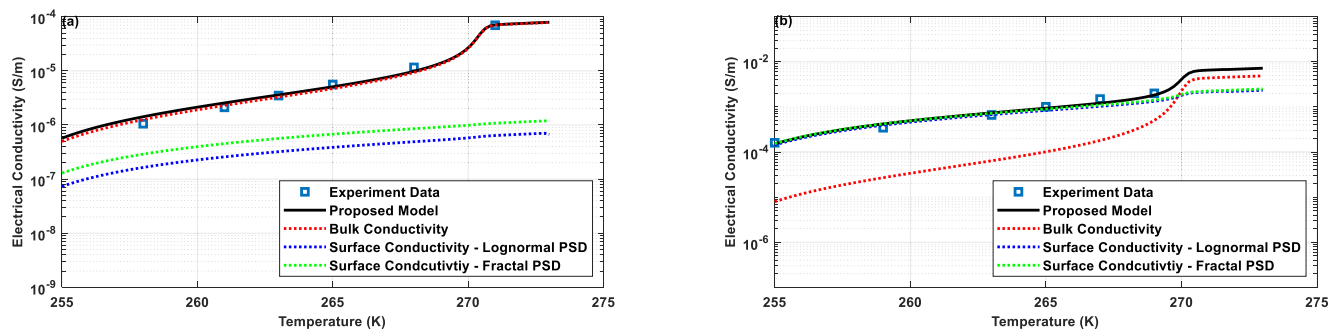
Figure 15. Evolution of the bulk conductivity and surface conductivity with different temperature values for lognormal and fractal pore size distributions. (a) Granite, initial concentration 0.0025 mol/L, Coperey, Revil, Abdulsamad et al. (2019); (b) NW sample, initial concentration 0.011 mol/L, Coperey, Revil, and Stutz (2019). The model parameters are given in Table 4(b) and 4(d).

upscaling procedure with lognormal and fractal PSDs. Finally, the expression of the effective formation factor is obtained from the proposed model of the electrical conductivity.

The sensitivity of the models with lognormal and fractal distributions has been tested. We explore wide ranges of values for microstructural parameters of the porous medium to quantify their influence on the electrical conductivity. From the model analysis, we observe that the model with lognormal PSD is mainly sensitive to the geometric mean pore radius r_m, but the model with fractal distribution is primary sensitive to the value of the smallest pore radius r_{min}, which means that parameter α (the ratio of the minimum pore radius to the maximum pore radius) has a different effect on the models. Besides, the proposed model can represent more capillary mechanisms (e.g., combination of the Gibbs-Thomson effect and surface complexation models) for the electrical conductivity of the porous medium than others available in the literature in frost state.

The proposed model successfully predicts the experimental data of electrical conductivity versus temperature of various types of samples from the experiments described in this work and published data. This physically-based
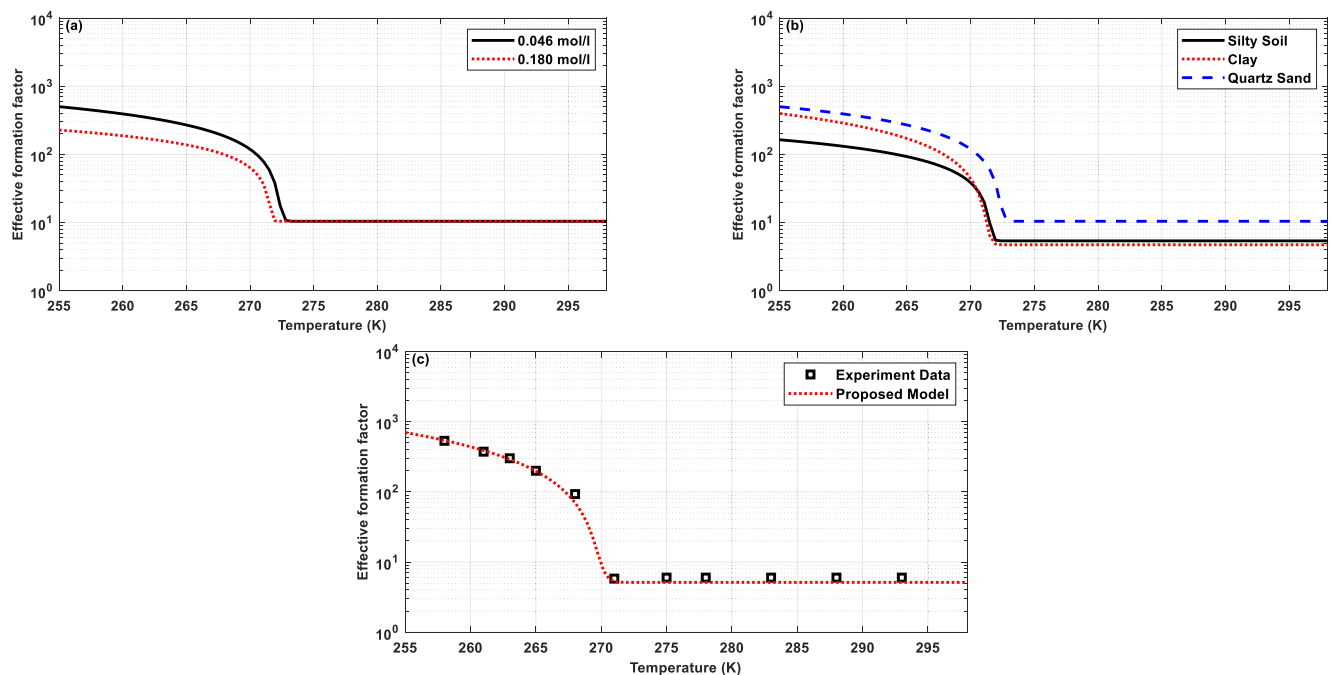
Figure 16. Evolution of the effective formation factor as a function of the temperature. (a) Effect of the electrolyte concentration on the effective formation factor. (b) Effect of different samples on the effective formation factor. (c) Comparison between the effective formation factor as a function of temperature (symbols) from Coperey, Revil, Abdulsamad et al. (2019, soil) and calculated by the proposed model (solid line). Model parameters are given in Table 4.

model with a lognormal or a fractal distributions can accurately fit the datasets. However, there are many physical parameters in the proposed model in this study. For instance, the second protonation and the relative equilibrium constant for the two types of interface are considered in the surface complexation models, but the laboratory measurements of electrical conductivity are in case of neutral pH (6–8), so we do not need to consider the second protonation equilibrium in the models in next time (it could be considered mostly from acid to very acid pH). Also, one could experimentally determine the PSD to determine the values of r_{min} and r_{max} to constrain and validate the model, and furthermore to reduce the numbers of the parameters of the physically-based model in future research.

We have considered the effect of bulk and surface conductivities in the proposed models. On the one hand, it is noted that surface conductivity decreases when the grain diameter increases, since samples with smaller particles have a larger specific surface than samples with bigger particles, while on the other hand, the surface conductivity is also sensitive to the CEC (the CEC). Additionally, from the proposed models, we obtain an expression for the effective formation factor that is explicitly linked with porosity, tortuosity and liquid water saturation. This expression for the effective formation factor is then well validated by published data. In the future, it will be important to extend this approach to partially saturated conditions in order to develop a unified model for application to a variety of complex environments. Moreover, we will take focus on extending the proposed model toward a broader temperature range (i.e., considering the temperature above the freezing temperature) in the following researches.

Appendix A: Experimental Data in This Study

This table shows the experimental data of liquid water saturation and electrical conductivity measured in this study at different temperatures and NaCl solute concentrations.

Sample	Porosity (ϕ)	Initial concentration (mol/L)	SFCC T (K)	SFCC S_u	Electrical conductivity T (K)	Electrical conductivity σ (S/m)
Clay	0.40	0.046	257	0.103		
			260	0.114		
			261	0.114	257	2.775E−04
			263	0.125	260	5.500E−04
			265	0.157	263	8.769E−04
			266	0.160	266	2.513E−03
			268	0.228	268	6.550E−03
			269	0.269	271	1.930E−02
			270	0.373		
			271	0.537		
			272	1.000		
Clay	0.40	0.180	257	0.121		
			260	0.136		
			261	0.153	257	1.494E−03
			263	0.182	260	2.373E−03
			265	0.199	263	4.436E−03
			267	0.275	266	1.151E−02
			268	0.294	268	1.977E−02
			269	0.419	270	4.702E−02
			270	0.552		
			271	1.000		

Sample	Porosity (ϕ)	Initial concentration (mol/L)	SFCC		Electrical conductivity	
			T (K)	S_u	T (K)	σ (S/m)
Silty soil	0.368	0.046	257	0.082		
			260	0.085	257	0.0016
			261	0.088	260	0.0022
			263	0.090	263	0.0031
			265	0.114	267	0.0053
			267	0.150	269	0.0077
			271	0.351	270	0.0128
			272	1.000		
Silty soil	0.368	0.180	257	0.108		
			260	0.112	257	0.0038
			261	0.114	260	0.0051
			263	0.121	263	0.0075
			265	0.132	266	0.0141
			267	0.167	270	0.0314
			270	0.281	271	0.0615
			271	0.541		
			272	1.000		
Quartz sand	0.240	0.046	257	0.057	257	1.136E−04
			260	0.060	260	1.606E−04
			265	0.079	263	2.486E−04
			268	0.109	268	7.339E−04
			272	0.410	270	2.343E−03
			273	1.000	272	7.588E−03
Quartz sand	0.240	0.180	257	0.122		
			260	0.126		
			261	0.134	257	1.311E−03
			263	0.137	260	2.081E−03
			265	0.143	263	3.300E−03
			267	0.145	268	7.571E−03
			270	0.214	270	1.250E−02
			271	0.394	272	4.030E−02
			272	1.000		

Notations

T	Temperature of the REV (K)
T_0	Freezing temperature of bulk liquid water (K)
T_m	Freezing temperature of the porous medium (K)
T_{ref}	Reference temperature (K)
ΔT_f	Shift in freezing point (K)
r	Radius of the capillary tube (m)
r_1	Radius of the capillary tube filled with liquid water (m)
r_2	Radius of the capillary tube occupied by bulk ice (m)
r_i	Critical freezing radius of the REV (m)
r_{max}	Maximum radius of the capillary tube (m)
r_{min}	Minimum radius of the capillary tube (m)

r_m	Geometric mean pore radius (m)
γ	Shape factor of the solid-liquid interface
σ_{sl}	Ice-liquid water interfacial free energy (J m^{-2})
σ_w	Electrical conductivity of pore water (S/m)
σ_s	Surface conductivity of the porous medium (S/m)
σ	Electrical conductivity of the porous medium (S/m)
σ_{eff}	Effective electrical conductivity of the porous medium (S/m)
L	Length of the sample (m)
L_f	Latent heat of phase transformation (J/kg)
L_e	Length of the capillary (the tortuous length) (m)
L_0	REV length (m)
ρ_i	Density of ice (kg m^{-3})
R	Resistance of the frozen saturated REV (Ω)
R_1	Resistance of the capillary ($r_{min} < r < r_i$) (Ω)
R_2	Resistance of the capillary ($r_i < r < r_{max}$) (Ω)
$R(r)$	Total resistance of the two types of capillary (Ω)
Σ	The conductance of the frozen saturated REV scale (S)
$\Sigma(r)$	The total conductance of the two capillaries (S)
Σ_s	Specific surface conductance (S)
Σ_{sw}	Specific surface conductance at the mineral-liquid water surface (S)
Σ_{iw}	Specific surface conductance at the bulk ice-liquid water surface (S)
A_{REV}	Cross-section area of REV (m^2)
$f(r)$	Capillary tube distribution function of the REV
F	Formation factor of the porous medium
F_{eff}	Effective formation factor of the porous medium
A	A normalizing prefactor
S	Area of the sample (m^2)
s	Log-normal standard deviation
N	Total number of capillaries
$N(\geq r)$	Number of the capillaries (with radius larger than r)
n	Unfrozen factor
ϕ	Porosity of the REV
V_P	Total pore volume (m^3)
V_{REV}	Total volume of the REV (m^3)
τ	Tortuosity
S_0	Initial saturation of the REV
S_u	Liquid water saturation of the REV
α	Ratio of the minimum pore radius to the maximum pore radius
$erf(z)$	Error function
D_f	Fractal dimension for pore space
a	Physical parameters of the SFCC
b	Physical parameters of the SFCC
c	Physical parameters of the SFCC
C_0	Initial ionic concentration of the REV (mol/L)
C_u	Ionic concentration of the REV in frost state (mol/L)
C_f	Salinity in the free electrolyte (mol/L)
$C_{H^+}^f$	Ionic concentration of the protons in the free electrolyte (mol/L)
$C_{Na^+}^f$	Ionic concentration of sodium cations in the free electrolyte (mol/L)
C_i^f	Concentration of ionic species i in the free electrolyte (mol/L)
N_A	Avogadro's number (mol^{-1})
q_i	Charge of species i in the free electrolyte (C)
β_i	Mobility of ionic species i in the free electrolyte (m^2 s^{-1} V^{-1})
β_i^{ref}	Reference mobility of ionic species i in the free electrolyte (m^2 s^{-1} V^{-1})
β_0^{ref}	Effective reference mobility (m^2 s^{-1} V^{-1})

α_T	Temperature factor (K^{-1})
Q_s^0	Surface charge density at the sum of the surface and the Stern layer (C)
Q_s	Surface charge density at the diffuse layer (C)
K_g	Geometrical dimensions of the sample (m)
K_{XOH}	Equilibrium constant of deprotonation at the solid surface-water interface
K_{XOH^2}	Equilibrium constant of protonation at the solid surface-water interface
K_{XONa}	Equilibrium constant of sodium adsorption at the solid surface-water interface
K_d	Equilibrium constant for deprotonation at the bulk ice-water interface
K_{HO}	Equilibrium constant for H$^+$ sorption at the bulk ice-water interface
K_{Na}	Equilibrium constant for sodium sorption at the bulk ice-water interface
K_p	Equilibrium constant for protonation
e_0	Elementary charge (C)
Γ_1^0	Total surface site density of the mineral (Sites nm^{-2})
Γ_s^0	Total surface site density of the ice (Sites nm^{-2})
φ_0	Surface potential (V)
φ_d	Stern potential (V)
ε_f	Permittivity of the pore water (F m^{-1})
k_b	Boltzmann's constant (J K^{-1})
C_1	Integral capacities of the Stern layer in the interface of the mineral-water (F m^{-2})
C_2	Integral capacities of the Stern layer at the bulk ice-water interface (F m^{-2})

Data Availability Statement

The experimental data used to estimate the electrical conductivity of saturated frozen porous media are accessible in open access in the Hydrogeophysics community of Zenodo and can be found at: https://doi.org/10.5281/zenodo.6606291.

References

Abu-Hassanein, Z. S., Benson, C. H., & Blotz, L. R. (1996). Electrical resistivity of compacted clays. *Journal of Geotechnical Engineering*, *122*(5), 397–406. https://doi.org/10.1061/(ASCE)0733-9410(1996)122:5(397)

Anderson, D. M. (1967). The interface between ice and silicate surfaces. *Journal of Colloid and Interface Science*, *25*(2), 174–191. https://doi.org/10.1016/0021-9797(67)90021-5

Anderson, D. M., & Hoekstra, P. (1965). Crystallization of clay-adsorbed water. *Science*, *149*(3681), 318–319. https://doi.org/10.1126/science.149.3681.318

Anderson, R., Tohidi, B., & Webber, J. B. W. (2009). Gas hydrate growth and dissociation in narrow pore networks: Capillary inhibition and hysteresis phenomena. *The Geological Society, London, Special Publications*, *319*(1), 145–159. https://doi.org/10.1144/SP319.12

Armistead, C. G., Tyler, A. J., Hambleton, F. H., Mitchell, S. A., & Hockey, J. A. (1969). Surface hydroxylation of silica. *Journal of Physical Chemistry*, *73*(11), 3947–3953. https://doi.org/10.1021/j100845a065

Aydin, M., Yano, T., & Kilic, S. (2004). Dependence of zeta potential and soil hydraulic conductivity on adsorbed cation and aqueous phase properties. *Soil Science Society of America Journal*, *68*(2), 450–459. https://doi.org/10.2136/sssaj2004.4500

Azmatch, T. F., Sego, D. C., Arenson, L. U., & Biggar, K. W. (2012). Using soil freezing characteristic curve to estimate the hydraulic conductivity function of partially frozen soils. *Cold Regions Science and Technology*, *83*(84), 103–109. https://doi.org/10.1016/j.coldregions.2012.07.002

Chalikakis, K., Plagnes, V., Guerin, R., Valois, R., & Bosch, F. P. (2011). Contribution of geophysical methods to karst-system exploration: An overview. *Hydrogeology Journal*, *19*(6), 1169–1180. https://doi.org/10.1007/s10040-011-0746-x

Clayton, W. S. (2017). In situ measurement of meltwater percolation flux in seasonal alpine snowpack using self-potential and capillary pressure sensors. In *The cryosphere discussions*. https://doi.org/10.5194/tc-2017-187

Clayton, W. S. (2021). Measurement of unsaturated meltwater percolation flux in seasonal snowpack using self-potential. *Journal of Glaciology*, *68*(267), 25–40. https://doi.org/10.1017/jog.2021.67

Collini, H., & Jackson, M. D. (2022). Relationship between zeta potential and wettability in porous media: Insights from a simple bundle of capillary tubes model. *Journal of Colloid and Interface Science*, *608*(1), 605–621. https://doi.org/10.1016/j.jcis.2021.09.100

Comiti, J., & Renaud, M. (1989). A new model for determining mean structure parameters of fixed beds from pressure drop measurements: Application to beds packed with parallelepipedal particles. *Chemical Engineering Science*, *44*(7), 539–1545. https://doi.org/10.1016/0009-2509(89)80031-4

Coperey, A., Revil, A., Abdulsamad, F., Stutz, B., Duvillard, P. A., & Ravanel, L. (2019). Low-frequency induced polarization of porous media undergoing freezing: Preliminary observations and modeling. *Journal of Geophysical Research: Solid Earth*, *124*(5), 4523–4544. https://doi.org/10.1029/2018JB017015

Coperey, A., Revil, A., & Stutz, B. (2019). Electrical conductivity versus temperature in freezing conditions: A field experiment using a basket geothermal heat exchanger. *Geophysical Research Letters*, *46*(24), 14531–14538. https://doi.org/10.1029/2019GL084962

Dafflon, B., Hubbard, S. S., Craig Ulrich, C., & Peterson, J. E. (2013). Electrical conductivity imaging of active layer and permafrost in an Arctic ecosystem, through advanced inversion of electromagnetic induction data. *Vadose Zone Journal*, *12*(4), 1–19. https://doi.org/10.2136/vzj2012.0161

Dafflon, B., Hubbard, S. S., Ulrich, C., Peterson, J. E., Wu, Y. X., Wainwright, H., & Kneafsey, T. J. (2016). Geophysical estimation of shallow permafrost distribution and properties in an ice-wedge polygon-dominated Arctic tundra region. *Geophysics*, *81*(1), WA247–WA263. https://doi.org/10.1190/geo2015-0175.1

Daigle, H. (2021). Structure of the electrical double layer at the ice-water interface. *Journal of Chemical Physics*, *154*(21), 214703. https://doi.org/10.1063/5.0048817

Debolskiy, M. V., Nicolsky, D. J., Hock, R., & Romanovsky, V. E. (2020). Modeling present and future permafrost distribution at the Seward Peninsula, Alaska. *Journal of Geophysical Research: Earth Surface*, *125*(8), e2019JF005355. https://doi.org/10.1029/2019JF005355

Delgado, A. V., Gonzalez-Caballero, F., Hunter, R. J., Koopal, L. K., & Lyklema, J. (2007). Measurement and interpretation of electrokinetic phenomena. *Journal of Colloid and Interface Science*, *309*(2), 194–224. https://doi.org/10.1016/j.jcis.2006.12.075

Duvillard, P. A., Magnin, F., Revil, A., Legay, A., Ravanel, L., Abdulsamad, F., & Coperey, A. (2021). Temperature distribution in a permafrost-affected rock ridge from conductivity and induced polarization tomography. *Geophysical Journal International*, *225*(2), 1207–1221. https://doi.org/10.1093/gji/ggaa597

Duvillard, P. A., Revil, A., Qi, Y., Soueid Ahmed, A., Coperey, A., & Ravanel, L. (2018). Three-dimensional electrical conductivity and induced polarization tomography of a rock glacier. *Journal of Geophysical Research: Solid Earth*, *123*(11), 9528–9554. https://doi.org/10.1029/2018JB015965

Fortier, R., LeBlanc, M. A., Allard, M., Buteau, S., & Calmels, F. (2008). Internal structure and conditions of permafrost mounds at Umiujaq in Nunavik, Canada, inferred from field investigation and electrical resistivity tomography. *Canadian Journal of Earth Sciences*, *45*(3), 367–387. https://doi.org/10.1139/E08-004

Glover, P. W. J. (2015). Geophysical properties of the near surface Earth: Electrical properties. *Treatise on Geophysics*, *11*, 89–137. https://doi.org/10.1016/B978-0-444-53802-4.00189-5

Glover, P. W. J., & Déry, N. (2010). Streaming potential coupling coefficient of quartz glass bead packs: Dependence on grain diameter, pore size, and pore throat radius. *Geophysics*, *75*(6), F225–F241. https://doi.org/10.1190/1.3509465

Guarracino, L., Rötting, T., & Carrera, J. (2014). A fractal model to describe the evolution of multiphase flow properties during mineral dissolution. *Advances in Water Resources*, *67*, 78–86. https://doi.org/10.1016/j.advwatres.2014.02.011

He, H., & Dyck, M. (2013). Application of multiphase dielectric mixing models for understanding the effective dielectric permittivity of frozen soils. *Vadose Zone Journal*, *12*(1), 1–22. https://doi.org/10.2136/vzj2012.0060

Herring, T., Cey, E., & Pidlisecky, A. (2019). Electrical resistivity of a partially saturated porous medium at Subzero temperatures. *Vadose Zone Journal*, *18*(1), 1–11. https://doi.org/10.2136/vzj2019.02.0019

Hiemstra, T., & Riemsdijk, W. H. V. (1990). Multiple activated complex dissolution of metal (hydr) oxides: A thermodynamic approach applied to quartz. *Journal of Colloid and Interface Science*, *136*(1), 132–150. https://doi.org/10.1016/0021-9797(90)90084-2

Ishizaki, T., Maruyama, M., Furukawa, Y., & Dash, J. G. (1996). Premelting of ice in porous silica glass. *Journal of Crystal Growth*, *163*(4), 455–460. https://doi.org/10.1016/0022-0248(95)00990-6

Jackson, M. D. (2008). Characterization of multiphase electrokinetic coupling using a bundle of capillary tubes model. *Journal of Geophysical Research*, *113*(B4), B04201. https://doi.org/10.1029/2007JB005490

Jackson, M. D. (2010). Multiphase electrokinetic coupling: Insights into the impact of fluid and charge distribution at the pore scale from a bundle of capillary tubes model. *Journal of Geophysical Research*, *115*(B7), 0148–0227. https://doi.org/10.1029/2009JB007092

Jin, X., Yang, W., Gao, X., Zhao, J. Q., Li, Z., & Jiang, J. (2020). Modeling the unfrozen water content of frozen soil based on the absorption effects of clay surfaces. *Water Resources Research*, *56*(12), e2020WR027482. https://doi.org/10.1029/2020WR027482

Jin, X. Y., Jin, H. J., Luo, D. L., Sheng, Y., Wu, Q. B., Wu, J. C., et al. (2022). Impacts of permafrost degradation on hydrology and vegetation in the source area of the Yellow River on Northeastern Qinghai-Tibet Plateau, Southwest China. *Frontiers of Earth Science*, *10*, 845824. https://doi.org/10.3389/feart.2022.845824

Jougnot, D., Ghorbani, A., Revil, A., Leroy, P., & Cosenza, P. (2010). Spectral induced polarization of partially saturated clay-rocks: A mechanistic approach. *Geophysical Journal International*, *180*(1), 210–224. https://doi.org/10.1111/j.1365-246X.2009.04426.x

Jougnot, D., Linde, N., Revil, A., & Doussan, C. (2012). Derivation of soil-specific streaming potential electrical parameters from hydrodynamic characteristics of partially saturated soils. *Vadose Zone Journal*, *11*(1), 272–286. https://doi.org/10.2136/vzj2011.0086

Jougnot, D., Roubinet, D., Guarracino, L., & Maineult, A. (2020). Modeling streaming potential in porous and fractured media, description and benefits of the effective excess charge density approach. In *Advances in modeling and interpretation in near surface geophysics: Springer geophysics series*.

Kallay, N., Čop, A., Chibowski, E., & Holysz, L. (2003). Reversible charging of the ice–water interface: II. Estimation of equilibrium parameters. *Journal of Colloid and Interface Science*, *259*(1), 89–96. https://doi.org/10.1016/S0021-9797(02)00179-0

Kemna, A., Weigand, M., & Zimmermann, E. (2014). Resistivity and SIP response of rocks during freezing and thawing. In *3rd international workshop on induced polarization (Oléron Island, France)*.

Koopmans, R. W. R., & Miller, R. D. (1966). Soil freezing and soil water characteristic curve. *Soil Science Society of America Journal*, *30*(6), 680–685. https://doi.org/10.2136/sssaj1966.03615995003000060011x

Kosugi, K. (1994). Three-parameter lognormal distribution model for soil water retention. *Water Resources Research*, *30*(4), 891–901. https://doi.org/10.1029/93WR02931

Kozlowski, T. (2007). A semi-empirical model for phase composition of water in clay–water systems. *Cold Regions Science and Technology*, *49*(3), 226–236. https://doi.org/10.1016/j.coldregions.2007.03.013

Kulessa, B., Chandler, D., Revil, A., & Essery, R. (2012). Theory and numerical modeling of electrical self-potential signatures of unsaturated flow in melting snow. *Water Resources Research*, *48*(9), W09511. https://doi.org/10.1029/2012WR012048

Kulessa, B., Hubbard, B., & Brown, G. H. (2003). Cross-coupled flow modeling of coincident streaming and electrochemical potentials and application to subglacial self-potential data. *Journal of Geophysical Research*, *108*(B8), 2381. https://doi.org/10.1029/2001JB001167

Lebeau, M., & Konrad, J. M. (2010). A new capillary and thin film flow model for predicting the hydraulic conductivity of unsaturated porous media. *Water Resources Research*, *46*(1), 1–15. https://doi.org/10.1029/2010WR009092

Lebeau, M., & Konrad, J. M. (2012). An extension of the capillary and thin film flow model for predicting the hydraulic conductivity of air-free frozen porous media. *Water Resources Research*, *48*(7), W07523. https://doi.org/10.1029/2012WR011916

Leroy, P., Devau, N., Revil, A., & Bizi, M. (2013). Influence of surface conductivity on the apparent zeta potential of amorphous silica nanoparticles. *Journal of Colloid and Interface Science*, *410*, 81–93. https://doi.org/10.1016/j.jcis.2013.08.012

Leroy, P., Jougnot, D., Revil, A., Lassin, A., & Azaroual, M. (2012). A double layer model of the gas bubble/water interface. *Journal of Colloid and Interface Science*, *388*(1), 243–256. https://doi.org/10.1016/j.jcis.2012.07.029

Leroy, P., Revil, A., Kemna, A., Cosenza, P., & Ghorban, A. (2008). Complex conductivity of water-saturated packs of glass beads. *Journal of Colloid and Interface Science*, *321*(1), 103–117. https://doi.org/10.1016/j.jcis.2007.12.031

Leroy, P., Tournassat, C., Bernard, O., Devau, N., & Azaroual, M. (2015). The electrophoretic mobility of montmorillonite. Zeta potential and surface conductivity effects. *Journal of Colloid and Interface Science*, *451*, 21–39. https://doi.org/10.1016/j.jcis.2015.03.047

Leroy, P., Tournassat, C., & Bizi, M. (2011). Influence of surface conductivity on the apparent zeta potential of TiO$_2$ nanoparticles. *Journal of Colloid and Interface Science*, *356*(2), 442–453. https://doi.org/10.1016/j.jcis.2011.01.016

Li, S., Leroy, P., Heberling, F., Devau, N., Jougnot, D., & Chiaberge, C. (2016). Influence of surface conductivity on the apparent zeta potential of calcite. *Journal of Colloid and Interface Science*, *468*, 262–275. https://doi.org/10.1016/j.jcis.2016.01.075

Li, S., Zhan, H., Lai, Y., Sun, Z., & Pei, W. (2014). The coupled moisture-heat process of permafrost around a thermokarst pond in Qinghai-Tibet Plateau under global warming. *Journal of Geophysical Research: Earth Surface*, *119*(4), 836–853. https://doi.org/10.1002/2013JF002930

Lyklema, J., & Minor, M. (1998). On surface conduction and its role in electrokinetics. *Colloids and Surfaces A: Physicochemical and Engineering Aspects*, *140*(1–3), 33–41. https://doi.org/10.1016/S0927-7757(97)00266-5

Mary, B., Peruzzo, L., Boaga, J., Cenni, N., Schmutz, M., Wu, Y., et al. (2020). Time-lapse monitoring of root water uptake using electrical resistivity tomography and missed-à-la-masse: A vineyard infiltration experiment. *Soils*, *6*(1), 95–114. https://doi.org/10.5194/soil-6-95-2020

Mendieta, A., Jougnot, D., Leroy, P., & Maineult, A. (2021). Spectral induced polarization characterization of non-consolidated clays for varying salinities—An experimental study. *Journal of Geophysical Research: Solid Earth*, *126*(4), e2020JB021125. https://doi.org/10.1029/2020JB021125

Ming, F., Li, D. Q., & Chen, L. (2020). Electrical resistivity of freezing clay: Experimental study and theoretical model. *Journal of Geophysical Research: Earth Surface*, *125*(2), e2019JF005267. https://doi.org/10.1029/2019JF005267

Murton, J. B., Kuras, O., Krautblatter, M., Cane, T., Tschofen, D., Uhlemann, S., et al. (2016). Monitoring rock freezing and thawing by novel geoelectrical and acoustic techniques. *Journal of Geophysical Research: Earth Surface*, *121*(12), 2309–2332. https://doi.org/10.1002/2016JF003948

Niu, Q., Revil, A., & Saidian, M. (2016). Salinity dependence of the complex surface conductivity of the Portland sandstone. *Geophysics*, *81*(2), 125–140. https://doi.org/10.1190/geo2015-0426.1

Oldenborger, G. A., & LeBlanc, A. (2018). Monitoring changes in unfrozen water content with electrical resistivity surveys in cold continuous permafrost. *Geophysical Journal International*, *72*(4), 177–187. https://doi.org/10.1093/gji/ggy321

Or, D., & Tuller, M. (1999). Liquid retention and interfacial area in variably saturated porous media: Upscaling from single-pore to sample-scale model. *Water Resources Research*, *35*(12), 3591–3605. https://doi.org/10.1029/1999WR900262

Pedrazas, M. N., Cardenas, M. B., Demir, C., Watson, J. A., Connolly, C. T., & McClelland, J. W. (2020). Absence of ice-bonded permafrost beneath an Arctic lagoon revealed by electrical geophysics. *Science Advances*, *6*(43), eabb5083. https://doi.org/10.1126/sciadv.abb5083

Pfannkuch, H. O. (1972). On the correlation of electrical conductivity properties of porous systems with viscous flow transport coefficients. *Developments in Soil Science*, *2*, 42–54. https://doi.org/10.1016/S0166-2481(08)70527-0

Pride, S. R., & Morgan, F. (1991). Electrokinetic dissipation induced by seismic waves. *Geophysics*, *56*(7), 914–925. https://doi.org/10.1190/1.1443125

Rembert, F., Jougnot, D., & Guarracino, L. (2020). A fractal model for the electrical conductivity of water-saturated porous media during mineral precipitation-dissolution processes. *Advances in Water Resources*, *145*, 103742. https://doi.org/10.1016/j.advwatres.2020.103742

Revil, A. (2012). Spectral induced polarization of shaly sands: Influence of the electrical double layer. *Water Resources Research*, *48*(2), W02517. https://doi.org/10.1029/2011WR011260

Revil, A. (2013). Effective conductivity and permittivity of unsaturated porous materials in the frequency range 1 mHz–1 GHz. *Water Resources Research*, *49*(1), 306–327. https://doi.org/10.1029/2012WR012700

Revil, A., Ahmed, A. S., & Matthai, S. (2018). Transport of water and ions in partially water-saturated porous media: Part 3. Electrical conductivity. *Advance in water Resources*, *121*, 97–111. https://doi.org/10.1016/j.advwatres.2018.08.007

Revil, A., Cathles, L. M., Losh, S., & Nunn, J. A. (1998). Electrical conductivity in shaly sands with geophysical applications. *Journal of Geophysical Research: Solid Earth*, *103*(B10), 23925–23936. https://doi.org/10.1029/98JB02125

Revil, A., Coperey, A., Shao, Z., Florsch, N., Fabricius, I. L., Deng, Y. P., et al. (2017). Complex conductivity of soils. *Water Resources Research*, *53*(8), 7121–7147. https://doi.org/10.1002/2017WR020655

Revil, A., & Glover, P. W. J. (1997). Theory of ionic-surface electrical conduction in porous media. *Physical Review* B, *55*(3), 1757–1773. https://doi.org/10.1103/PhysRevB.55.1757

Revil, A., Karaoulis, M., Johnson, T., & Kemna, A. (2012). Review: Some low-frequency electrical methods for subsurface characterization and monitoring in hydrogeology. *Hydrogeology Journal*, *20*(4), 617–658. https://doi.org/10.1007/s10040-011-0819-x

Schuur, E., McGuire, A., Schädel, C., Grosse, G., Harden, J. W., Hayes, D. J., et al. (2015). Climate change and the permafrost carbon feedback. *Nature*, *520*(7546), 171–179. https://doi.org/10.1038/nature14338

Shan, W., Liu, Y., Hu, Z. G., & Xiao, J. T. (2015). A model for the electrical resistivity of frozen soils and an experimental verification of the model. *Cold Regions Science and Technology*, *119*, 75–83. https://doi.org/10.1016/j.coldregions.2015.07.010

Shen, Y., Wang, Y., Wei, X., Jia, H., & Yan, R. (2020). Investigation on meso-debonding process of the concrete interface induced by freeze-thaw cycles using NMR technology. *Construction and Building Materials*, *252*, 118962. https://doi.org/10.1016/j.conbuildmat.2020.118962

Suits, L. D., Sheahan, T. C., Scholte, J. W., Shang, J. Q., & Rowe, R. K. (2002). Improved complex permittivity measurement and data processing technique for soil-water systems. *Geotechnical Testing Journal*, *25*(2), 187–198. https://doi.org/10.1520/GTJ11362J

Tan, L., Wei, C., Tian, H. H., Zhou, J., & Wei, H. (2015). Experimental study of unfrozen water content of frozen soils by low-field nuclear magnetic resonance. *Rock and Soil Mechanics*, *36*(6), 1566–1572. https://doi.org/10.16285/j.rsm.2015.06.006

Tang, L. Y., Wang, K., Jin, L., Yang, G. S., Jia, H. L., & Taoum, A. (2018). A resistivity model for testing unfrozen water content of frozen soil. *Cold Regions Science and Technology*, *153*, 55–63. https://doi.org/10.1016/j.coldregions.2018.05.003

Tang, R., Zhou, G., Jiao, W., & Ji, Y. (2019). Theoretical model of hydraulic conductivity for frozen saline/non-saline soil based on freezing characteristic curve. *Cold Regions Science and Technology*, *165*, 102794. https://doi.org/10.1016/j.coldregions.2019.102794

Teng, J. D., Kou, J. Y., Yan, X., Zhang, S., & Sheng, D. C. (2020). Parameterization of soil freezing characteristic curve for unsaturated soils. *Cold Regions Science and Technology*, *170*(68), 102928. https://doi.org/10.1016/j.coldregions.2019.102928

Teng, J. D., Liu, J. L., Zhang, S., & Sheng, D. C. (2020). Modelling frost heave in unsaturated coarse-grained soils. *Acta Geotechnica*, *15*(11), 3307–3320. https://doi.org/10.1007/s11440-020-00956-2

Teng, J. D., Yan, H., Liang, S. H., Zhang, S., & Sheng, D. C. (2021). Generalizing the Kozeny-Carman equation to frozen soils. *Journal of Hydrology*, *594*, 125885. https://doi.org/10.1016/j.jhydrol.2020.125885

Thanh, L. D., Jougnot, D., Solazzi, S. G., Van Do, P., & Van Do, P. (2021). Dynamic streaming potential coupling coefficient in porous media with different pore size distributions. *Geophysical Journal International*, *229*(1), 720–735. https://doi.org/10.1093/gji/ggab491

Thanh, L. D., Jougnot, D., Van Do, P., Tuyen, V. P., Ca, N. X., & Hien, N. T. (2020). A physically based model for the electrical conductivity of partially saturated porous media. *Geophysical Journal International*, *223*(2), 993–1006. https://doi.org/10.1093/gji/ggaa307

Thanh, L. D., Jougnot, D., Van Do, P., & Van Nghia, A. N. (2019). A physically based model for the electrical conductivity of water-saturated porous media. *Geophysical Journal International*, *219*(2), 866–876. https://doi.org/10.1093/gji/ggz328

Tuller, M., & Or, D. (2001). Hydraulic conductivity of variably saturated porous media: Film and corner flow in angular pore space. *Water Resources Research*, *37*(5), 1257–1276. https://doi.org/10.1029/2000WR900328

Tyler, S. W., & Wheatcraft, S. W. (1990). Fractal processes in soil water retention. *Water Resources Research*, *26*(5), 1047–1054. https://doi.org/10.1029/WR026i005p01047

Vinegar, H. J., & Waxman, M. H. (1984). Induced polarization of shaly sands. *Geophysics*, *49*(8), 1267–1287. https://doi.org/10.1190/1.1441755

Vinogradov, J., Hill, R., & Jougnot, D. (2021). Influence of pore size distribution on the electrokinetic coupling coefficient in two-phase flow conditions. *Water*, *13*(17), 2316. https://doi.org/10.3390/w13172316

Walvoord, M. A., & Kurylyk, B. L. (2016). Hydrologic impacts of thawing permafrost—A review. *Vadose Zone Journal*, *15*(6), 1–20. https://doi.org/10.2136/vzj2016.01.0010

Wang, C., Lai, Y., & Zhang, M. (2017). Estimating soil freezing characteristic curve based on pore-size distribution. *Applied Thermal Engineering*, *124*, 1049–1060. https://doi.org/10.1016/j.applthermaleng.2017.06.006

Wang, T., Li, P., Liu, Y., Hou, J. M., Li, Z. B., Ren, Z. P., et al. (2020). Experimental investigation of freeze–thaw meltwater compound erosion and runoff energy consumption on loessal slopes. *Catena*, *185*, 104310. https://doi.org/10.1016/j.catena.2019.104310

Watanabe, K., & Flury, M. (2008). Capillary bundle model of hydraulic conductivity for frozen soil. *Water Resources Research*, *44*(12), W12402. https://doi.org/10.1029/2008WR007012

Watanabe, K., & Mizoguchi, M. (2002). Amount of unfrozen water in frozen porous media saturated with solution. *Cold Regions Science and Technology*, *34*(2), 103–110. https://doi.org/10.1016/S0165-232X(01)00063-5

Watanabe, K., & Osada, Y. (2016). Comparison of hydraulic conductivity in frozen saturated and unfrozen unsaturated soils. *Vadose Zone Journal*, *15*(5), 1–7. https://doi.org/10.2136/vzj2015.11.0154

Watanabe, K., & Wake, T. (2009). Measurement of unfrozen water content and relative permittivity of frozen unsaturated soil using NMR and TDR. *Cold Regions Science and Technology*, *59*(1), 41. https://doi.org/10.1016/j.coldregions.2009.05.011

Watlet, A., Kaufmann, O., Triantafyllou, A., Poulain, A., Chambers, J. E., Meldrum, P. I., et al. (2018). Imaging groundwater infiltration dynamics in the karst vadose zone with long-term ert monitoring. *Hydrology and Earth System Sciences*, *22*(2), 1563–1592. https://doi.org/10.5194/hess-22-1563-2018

Waxman, M. H., & Smits, L. J. M. (1968). Electrical conductivities in oil-bearing shaly sands. *Society of Petroleum Engineers Journal*, *8*(02), 107–122. https://doi.org/10.2118/1863-A

Winsauer, W. O., Shearin, H. M., Masson, P. H., & Williams, M. (1952). Resistivity of brine-saturated sands in relation to pore geometry. *AAPG Bulletin*, *36*(2), 253–277. https://doi.org/10.1306/3D9343F4-16B1-11D7-8645000102C1865D

Woodruff, W. F., & Revil, A. (2011). CEC-normalized clay-water sorption isotherm. *Water Resources Research*, *47*(11), W11502. https://doi.org/10.1029/2011WR010919

Xu, X. Z., Wang, J. C., & Zhang, L. X. (2001). *Frozen soil physics*. Beijing Science and Technology Press.

Yang, Z., Lv, J., Shi, W., Jia, C., Wang, C., Hong, Y., & Ling, X. Z. (2021). Experimental study of the freeze thaw characteristics of expansive soil slope models with different initial moisture contents. *Scientific Reports*, *11*(1), 23177. https://doi.org/10.1038/s41598-021-02662-9

Yoshikawa, K., & Overduin, P. P. (2005). Comparing unfrozen water content measurements of frozen soil using recently developed commercial sensors. *Cold Regions Science and Technology*, *42*(3), 250–256. https://doi.org/10.1016/j.coldregions.2005.03.001

Yu, B., & Cheng, P. (2002). A fractal permeability model for bi-dispersed porous media. *International Journal of Heat and Mass Transfer*, *45*(14), 2983–2993. https://doi.org/10.1016/S0017-9310(02)00014-5

Yu, B., Lee, L. J., & Cao, H. (2001). Fractal characters of pore microstructures of textile fabrics. *Fractals*, *09*(02), 155–163. https://doi.org/10.1142/S0218348X01000610

Zhou, J., Wei, C., Lai, Y., Wei, H., & Tian, H. (2018). Application of the generalized Clapeyron Equation to freezing point depression and unfrozen water content. *Water Resources Research*, *54*(11), 9412–9431. https://doi.org/10.1029/2018WR023221

Zhou, X. H., Zhou, J., Kinzelbach, W., & Stauffer, F. (2014). Simultaneous measurement of unfrozen water content and ice content in frozen soil using gamma ray attenuation and TDR. *Water Resources Research*, *50*(12), 9630–9655. https://doi.org/10.1002/2014WR015640

Zimmermann, R., Dukhin, S., & Werner, C. (2001). Electrokinetic measurements reveal interfacial charge at polymer films caused by simple electrolyte ions. *The Journal of Physical Chemistry B*, *105*(36), 8544–8549. https://doi.org/10.1021/jp004051u